## Reynolds number scaling of burning rates in spherical turbulent premixed flames

Journal:	Journal of Fluid Mechanics
Manuscript ID	JFM-19-S-1558
mss type:	JFM Papers
Date Submitted by the Author:	09-Oct-2019
Complete List of Authors:	Kulkarni, Tejas; University of Texas at Austin Cockrell School of Engineering, Department of Aerospace Engineering and Engineering Mechanics Attili, Antonio; RWTH Aachen University Institute of Combustion Technologies Bisetti, Fabrizio; University of Texas at Austin Cockrell School of Engineering, Department of Aerospace Engineering and Engineering Mechanics
Keyword:	Turbulent reacting flows < Reacting Flows, Isotropic turbulence < Turbulent Flows

SCHOLARONE™ Manuscripts

# Reynolds number scaling of burning rates in spherical turbulent premixed flames

## Tejas Kulkarni<sup>1</sup>† Antonio Attili<sup>2</sup> and Fabrizio Bisetti<sup>1</sup>

<sup>1</sup>Department of Aerospace Engineering and Engineering Mechanics The University of Texas at Austin, Austin, TX 78712, USA <sup>2</sup>Institute for Combustion Technology RWTH Aachen University, Aachen, Germany

(Received xx; revised xx; accepted xx)

Turbulent burning rates are several times higher than their laminar counterparts. In the flamelet regime of turbulent premixed combustion, numerical and experimental studies have shown that enhancements in the burning rates originate primarily from surface wrinkling, while local burning is laminar-like. In this work, we simulate spherical turbulent premixed methane/air flames in decaying isotropic turbulence at various Reynolds numbers and analyse the data using the surface density function formalism. Surface wrinkling is quantified in terms of the area ratio, defined as the ratio of the area of the turbulent flame surface to a reference area. The area ratio is shown to be proportional to the product of the turbulent flame brush thickness and the peak value of the surface density function. Because the thickness is proportional to the integral length scale of turbulence and the surface density is proportional to the inverse of a length scale close to the Taylor microscale, the area ratio and the burning rate are found to increase with  $Re_{\lambda}^{1.13}$ .

#### Key words:

#### 1. Introduction

Technical combustion devices operate in the turbulent regime in order to increase burning rates and achieve higher power densities than are otherwise possible in laminar flows. In most laboratory experiments and numerical simulations of turbulent premixed flames, the primary mechanism responsible for the enhancement in burning rates is flame wrinkling by turbulence (Driscoll 2008).

A flame is a thin region of space where chemical reactions convert reactants into products and a premixed flame is most often approximated as an interface propagating into the unburnt gases (Peters 2000). In most theoretical constructs, the flame interface is taken to coincide with an iso-surface of the reaction progress variable (Pope 1988), which is defined as a normalized reactive scalar field varying monotonically across the flame from zero in the reactants to unity in the products. Instantaneously, the iso-surface propagates in the direction of its normal with a relative speed set by the local balance between chemical reactions and diffusive transport (Williams 1994). The relative speed is referred to as displacement speed.

Unsteady, three-dimensional turbulent fluid motion wrinkles, folds, stretches, and

† Email address for correspondence: tukulkarni@utexas.edu

compresses the flame surface, causing an increase of its area on average. Because of the greater area, more mixture is processed as the flame propagates into unburnt reactants, leading to increased overall burning rates in the presence of turbulence (Damköhler 1940). The concept of a propagating surface lies at the basis of several closures for turbulent premixed combustion, such as the level set method (Williams 1985; Peters 2000), the flame surface density (Marble & Broadwell 1977; Pope 1988; Candel & Poinsot 1990), and the extended flame surface density (Veynante & Vervisch 2002).

In this work, we are concerned with the statistics and evolution of the surface area of spherically expanding turbulent premixed flames and associated burning rates. We explore how *scale separation* affects the growth and development of the turbulent flame surface area. By scale separation, we mean the most distinguishing feature of a turbulent flow, whereby spatial and temporal scales are organized over a range that widens with increasing Reynolds number (Frisch 1995). The following questions motivate our work: Does scale separation, as parametrized by the Reynolds number, affect the burning rates of turbulent premixed flames? If so, what are the mechanisms?

## 1.1. Scaling of turbulent burning rates

It is commonly assumed that the dimensionless turbulent flame speed  $S_T/S_L$  depends primarily on the ratio  $u'/S_L$ . Here u' is the turbulent velocity fluctuation,  $S_L$  is the displacement speed for a freely propagating laminar flame, and the turbulent flame speed  $S_T/S_L$  is a dimensionless mean burning rate defined based on the volumetric integral of the rate of consumption of fuel. Within this theoretical framework, first proposed by Damköhler for large scale turbulence (Damköhler 1940), the ratio  $l/\delta_L$ , where l is the integral scale and  $\delta_L$  is the flame thermal thickness, does not play a role in controlling mean burning rates. Yet, there exists experimental evidence that suggest a far more complex dependence of  $S_T/S_L$  on the properties of turbulence and the Reynolds number in particular.

Liu et al. (2012) investigated the dependence of turbulent flame speeds in pressurized premixed methane/air mixtures propagating in homogeneous isotropic turbulence up to  $Re_{\lambda} \approx 100$ . By controlling independently u' and l (via fan speed) and the reactants' kinematic viscosity  $\nu$  (via pressure), the authors were able to measure burning rates for various values of  $u'/S_L$ , while holding  $Re_{\lambda}$  constant and experiments were repeated for several values of the Reynolds number. The turbulent flame speed  $S_T/S_L$  was found to increase with Reynolds number, remaining nearly constant as  $u'/S_L$  varied. Data across multiple experiments suggest that the Reynolds number, not  $u'/S_L$ , is the primary controlling parameter in spherical turbulent premixed flames.

Kobayashi et al. (1996, 2005) measured mean burning rates in pressurized Bunsen burners equipped with turbulence generating grids, finding increasing values of  $S_T/S_L$  for increasing pressures at constant values of  $u'/S_L$ . Since  $u'/S_L$  was held constant alongside the geometry of the burner and grids, giving a nearly constant integral scale l also, the increase in  $S_T/S_L$  may be due to the increase in Reynolds number brought by the decreasing kinematic viscosity with increasing pressure.

Theoretical support for the dependence of turbulent burning rates on the Reynolds number was recently presented by Chaudhuri et al. (2011). Starting from the spectral closure of the level-set equation (Peters 1992), Chaudhuri et al. (2011) proposed and later confirmed experimentally (Chaudhuri et al. 2012) a  $Re^{1/2}$  scaling for  $S_T/S_L$  in turbulent spherical premixed flames, where Re is based on the turbulent flame radius and the reactants' thermal diffusivity. The authors' experimental evidence in favour of

a  $Re^{1/2}$  scaling includes measurements for a variety of reactive mixtures, pressures, and turbulence parameters.

Finally, numerous experimental studies of turbulent spherical premixed flames at the University of Leeds postulated and explored the dependence of  $S_T/S_L$  from  $Re \sim u'l$  or  $Re_{\lambda} \sim u'\lambda$  (Andrews et al. 1975; Abdel-Gayed & Bradley 1977; Abdel-Gayed et al. 1981), although this proposition was later deferred in favour of relating turbulent flame speeds to  $u'/S_L$  instead.

#### 1.2. Theoretical framework for the Reynolds scaling

Theoretical arguments in support of the dependence of the turbulent flame speed  $S_T/S_L$  (or dimensionless mean burning rate) from the Reynolds number are possible and will be put forth within the formalism of the surface density function. Briefly, the surface density function (SDF) is a statistical measure of the area of a surface per unit volume. For turbulent premixed flames, the SDF characterizes the statistics of the area of a wrinkled flame and overall burning rate. The turbulent flame brush is the region of space where the flame is most likely to be located and the SDF is found to peak in the middle of the brush, decreasing rapidly on its periphery (Driscoll 2008).

It can be shown that the mean area of a turbulent premixed flame is proportional to the product of the peak value of the SDF across the brush and the linear extent of the brush, or its thickness. In other words, all other quantities being equal, the greater the value of the peak SDF and the wider the brush, the greater the mean flame surface area and the higher the burning rates of the turbulent flame.

The flame brush thickness is defined as the inverse of the peak gradient magnitude of the mean progress variable. Because the location of the flame brush and its thickness depend on the mean progress variable field and its gradient, we may expect the flame brush to depend primarily on the largest scales of turbulent fluid motion, the geometry of the flow, and boundary and initial conditions (Lawn & Schefer 2006). For example, in the case of a Bunsen burner, the brush thickness scales linearly with the diameter of the nozzle (Lipatnikov & Chomiak 2002), all other relevant dimensionless parameters held constant. In other words, the turbulent flame brush thickness is proportional to the largest scales of the flow and largely independent of the Reynolds number. Such behavior is characteristic of other turbulent flows for which the spatial distribution of the normalized mean velocity, passive scalar, and their fluctuations do not depend markedly on the Reynolds number of the flow, e.g. turbulent round jets (Pope 2000).

The relationship between the brush thickness and the integral scale of the flow becomes clear if Taylor's theory of turbulent diffusion of material points (Taylor 1922) is applied to the evolution of the turbulent flame brush thickness (Lipatnikov 2012). Within the confines of the analysis, the thickness scales with the integral length scale as verified experimentally and via direct numerical simulations of turbulent premixed flames (Lipatnikov 2012).

The flame surface density function is the second quantity of interest to the argument that burning rates increase with increasing Reynolds number. As mentioned, the SDF is a statistical quantity representing the expectation of the area of the flame surface per unit volume (Vervisch et al. 1995) and is found to reach its maximum in the middle of the turbulent flame brush, decaying rapidly to zero outside of the brush itself (Driscoll 2008; Veynante & Vervisch 2002). When the flame surface is taken to coincide with a specific iso-surface of the progress variable (Pope 1988), the SDF obeys a transport equation (Vervisch et al. 1995; Trouvé & Poinsot 1994), which includes terms that describe turbulent transport by velocity fluctuations, transport by flame propagation, and

production and destruction of flame surface by two processes, one kinematic and the other associated with flame propagation in the presence of curvature. Data from experiments and simulations suggest that the rates of flame surface production and destruction may be proportional to the inverse of the Kolmogorov time scale  $\tau_{\eta}$  (Luca *et al.* 2018b).

The kinematic mechanism applies to propagating and material surfaces alike as velocity gradients induce positive (stretch) and negative (compression) tangential strain on the surface. It is well known (Batchelor 1952; Cocke 1969) that tangential strain on surfaces is, on average, positive, so that surface elements in turbulent flows are preferentially stretched and flattened, leading to an increase in their area (Girimaji & Pope 1990; Drummond & Münsch 1990; Girimaji & Pope 1992; Drummond 1993; Tabor & Klapper 1994). This result is connected with the statistics of the alignment of the principal eigenvectors of the velocity gradient tensor with the normal to the surface.

The surface normal is aligned preferentially with the eigenvector associated with the most compressive eigenvalue of the rate of strain tensor (Tsinober 2009). The alignment statistics and preferential stretching of surfaces are universal across diverse turbulent flows and so robust that they occur even in Gaussian random velocity fields, i.e. surface stretching does not require the velocity field to be the solution to the Navier-Stokes equations (Tsinober 2009). Further, Attili & Bisetti (2019) showed that the mixture fraction field displays the same alignment statistics in turbulent nonpremixed jet flames as in many other isothermal turbulent flows with or without mean shear (Ashurst et al. 1987; She et al. 1991; Tsinober et al. 1992; Vincent & Meneguzzi 1994).

In homogeneous isotropic turbulence, the mean rate of tangential stretch of infinitesimal material surface elements was shown to scale with the inverse of  $\tau_{\eta}$ , independently of the Reynolds number (Girimaji & Pope 1990). The same Kolmogorov scaling was found to hold for the net rate of tangential strain of the surface of turbulent premixed jet flames over a range of Reynolds numbers (Luca et al. 2018b), implying that the kinematic mechanism may apply to surfaces in turbulent flows with density gradients and variable transport properties also. Experiments with spherically expanding turbulent flames with varying density ratios, defined as the ratio between the density of the unburnt to burnt gases, demonstrated that turbulent flame speeds are not affected significantly by the density ratio (Lipatnikov et al. 2017), further supporting the conclusion that mechanisms of surface generation by stretch may be largely insensitive to density gradients.

The second mechanism contributing to the generation and destruction of flame surface requires propagation in the presence of curvature and the rate of change of the surface area is proportional to the product of the displacement speed and the curvature of the surface (Candel & Poinsot 1990). The propagative mechanism is responsible for the destruction of surface area on average as confirmed by recent data from direct numerical simulations of planar (Nivarti & Cant 2017) and jet (Luca et al. 2018b) turbulent premixed flames.

The scaling of the propagative term, which is proportional to the product of the local flame curvature and displacement speed, is far from established, although data from simulations of turbulent premixed jet flames suggest that the net rate of destruction of flame surface by the propagative mechanism may be proportional to the inverse of the Kolmogorov time scale (Luca *et al.* 2018b).

Numerical studies of the curvature of infinitesimal material surface elements showed that the first five moments of the probability density function of curvature scale with the Kolmogorov length scale to a very good approximation (Girimaji 1991). Support for a relation between curvature and the surface density function in turbulent flames was advanced by Huh *et al.* (2013), who argued that the peak value of the surface density

function is proportional to the mean of the absolute value of the flame curvature and investigated such postulate via simulations of statistically stationary planar turbulent premixed flames. The mean magnitude of the curvature was shown to scale proportionally to the inverse of the Kolmogorov length scale in agreement with Girimaji (1991). Similar results for the statistics of curvature of propagating surfaces in isotropic turbulence were reported by Zheng et al. (2017) also. Despite the lack of a comprehensive theory, it appears reasonable to expect that the smallest scales of turbulence and their characteristic time are involved in the propagative mechanism.

If surface generation and destruction occur at the smallest scales of the flow, it is possible that the entire spectrum of turbulence contributes to the wrinkling, stretching, and folding of surfaces. Further support for this hypothesis comes from the fractal geometry of interfaces and scalar iso-surfaces in turbulence (Mandelbrot 1975; Sreenivasan & Meneveau 1986; Sreenivasan 1991). Recent experiments focusing on the turbulent/nonturbulent (T/NT) interface in a turbulent boundary layer at high Reynolds number have shown conclusively that the T/NT interface is fractal with power-law behaviour over nearly two decades in the inertial range (de Silva et al. 2013). Thus, the geometrical features of an interface embedded in a turbulent field reflect all motions of turbulence in the inertial range, down to a fractal cut-off length scale similar in size to the Kolmogorov length.

It is very likely that turbulent premixed flames possess a similar fractal nature (Gouldin 1987; Chatakonda *et al.* 2013), although available data are not conclusive on the account of the modest values of the Reynolds number and limited scale separation, which make it difficult to identify power laws and fractal dimension.

Based on the discussion above, the thickness of the brush of a turbulent premixed flame is found to scale proportionally to the integral scale of the flow, while there is evidence that rates of surface generation (and destruction) may increase as the dissipative scales of turbulence become smaller. Thus, it is certainly possible that the higher the Reynolds number and the broader the separation between the large and small scales of turbulence, the greater the value of the dimensionless product between the brush thickness and the peak SDF, leading to greater values of  $S_T/S_L$  and enhancement to the burning rates.

#### 1.3. Spherical turbulent premixed flames

We explore the above postulate with Direct Numerical Simulations (DNS) of spherical turbulent premixed flames in decaying isotropic turbulence at various values of the Reynolds number. The flame configurations have low values of the Karlovitz number, so that turbulent combustion occurs in the flamelet limit (Peters 2000; Libby & Williams 1994; Libby & Bray 1980), where modifications to flame propagation are negligible (Driscoll 2008).

Spherical turbulent premixed flames are a canonical configuration in the experimental study of turbulent premixed combustion (Fairweather et al. 2009; Renou et al. 2002; Liu et al. 2012; Chaudhuri et al. 2012). In a typical setup, a closed vessel is filled with premixed reactants and the mixture is stirred by fans. When arranged properly, the fans generate nearly homogeneous and isotropic turbulence in the centre of the vessel, where a spark ignites the reactive mixture. The flame propagates outwards into the reactants as its surface is wrinkled by turbulence. Most often, the fans are operating during flame propagation, so that turbulence in the reactants is nearly statistically stationary.

For the purpose of conducting numerical simulations, this configuration offers the following two advantages. Firstly, the turbulent statistics are a function of time and radial distance from the centre of the spherical flame only, so that ensemble averages

are gathered over the polar and azimuthal angles at each instant in time. Secondly, the statistical state of turbulence encountered by the propagating flame is characterized by the velocity fluctuation u', integral length scale l, and kinematic viscosity  $\nu$ . Further, the Reynolds number based on the Taylor microscale  $Re_{\lambda}$  is a unique measure of the ratio of the integral to the Kolmogorov scales.

The rest of the article is organized as follows. §2 describes the governing equations and numerical methods. The configuration is presented in §3. The temporal evolution of integral properties of the turbulent flames, such as burning rates, flame radius, and flame surface area are discussed in §4. §5 presents the analysis of the evolution of the peak surface density function and turbulent flame brush thickness. Scaling laws are proposed for both quantities separately in §6 and a scaling law for the evolution of the flame area ratio as a function of the Reynolds number is discussed. The article concludes in §7 with a summary of the results and prominent findings.

## 2. Governing equations

The evolution of the flow is described by the reactive multi-component Navier-Stokes equations in the low Mach number limit (Tomboulides *et al.* 1997; Mueller 1999). The continuity and momentum equations read

$$\frac{D\rho}{Dt} = -\rho \nabla \cdot \boldsymbol{u} \tag{2.1}$$

and

$$\rho \frac{D\boldsymbol{u}}{Dt} = -\nabla \pi + \nabla \cdot \boldsymbol{T},\tag{2.2}$$

respectively. Here  $D/Dt = \partial/\partial t + \boldsymbol{u} \cdot \nabla$  denotes the material derivative, where  $\boldsymbol{u}$  is the mass averaged bulk velocity (Bird et al. 2006). In the momentum equation,  $\boldsymbol{T}$  is the viscous shear stress tensor and  $\pi = \pi(\boldsymbol{x},t)$  is the hydrodynamic pressure, which is small compared to the spatially homogeneous background thermodynamic pressure p = p(t). The mixture density  $\rho$  obeys the equation of state for a mixture of ideal gases

$$p = \rho \mathcal{R}T/W, \tag{2.3}$$

where  $\mathcal{R}$  is the universal gas constant and W the molar mass of the mixture and T is temperature. Thus, spatial variations in density are related to spatial variations in temperature and mixture composition, but not in pressure.

A Newtonian fluid model is used for closure of the viscous shear stress tensor

$$\mathbf{T} = \mu \left( \nabla \mathbf{u} + (\nabla \mathbf{u})^T \right) - \frac{2}{3} \mu (\nabla \cdot \mathbf{u}) \mathbf{I}, \tag{2.4}$$

where  $\nabla u$  is the velocity gradient tensor and I is the identity tensor. A mixture averaged model is employed for the dynamic viscosity of the mixture  $\mu$  (Wilke 1950; Bird *et al.* 2006).

The species densities are  $\rho_i = \rho Y_i$ , where  $Y_i$  is the mass fraction of the *i*-th species, and obey the following transport equations (i = 1, ..., M)

$$\rho \frac{DY_i}{Dt} = -\nabla \cdot (\rho_i \mathbf{V}_i) + \omega_i \,, \tag{2.5}$$

where  $\omega_i$  and  $V_i$  refer to the net rate of production of species i due to chemical reactions and the mass diffusion velocity, respectively. Diffusive transport of species is modelled with the Hirschfelder-Curtiss approximation (Hirschfelder *et al.* 1954; Poinsot

Reynolds scaling of turbulent burning rates

& Veynante 2012)

$$\mathbf{V}_i X_i = -\mathcal{D}_i \nabla X_i, \tag{2.6}$$

where

$$\mathcal{D}_{i} = (1 - Y_{i}) / \left( \sum_{\substack{j=1\\j \neq i}}^{M} X_{j} / \mathcal{D}_{ij} \right).$$
 (2.7)

 $X_i$  denotes the mole fraction of the *i*-th species. In the above equations,  $\mathcal{D}_{ij}$  and  $\mathcal{D}_i$  are the binary and species diffusion coefficients, respectively. Closure for the mass diffusion velocity reads

$$\rho_i \mathbf{V}_i = -\rho \mathcal{D}_i \frac{Y_i}{X_i} \nabla X_i = -\rho \mathcal{D}_i \frac{\nabla (WY_i)}{W}. \tag{2.8}$$

This approximation is complemented by a small correction velocity  $u^c$  in order to ensure total mass conservation, yielding

$$\frac{\partial \rho_i}{\partial t} + \nabla \cdot (\rho_i \left( \boldsymbol{u} + \boldsymbol{u}^c \right)) = -\nabla \cdot (\rho_i \boldsymbol{V}_i) + \omega_i, \tag{2.9}$$

where

$$u^{c} = -\sum_{i=1}^{M} Y_{i} V_{i} = \sum_{i=1}^{M} \mathcal{D}_{i} Y_{i} \frac{\nabla W}{W} + \sum_{i=1}^{M} \mathcal{D}_{i} \nabla Y_{i}.$$
 (2.10)

The equation for the conservation of enthalpy is manipulated into a differential equation for temperature

$$\rho c_p \frac{DT}{Dt} = \frac{dp}{dt} + \nabla \cdot (\Lambda \nabla T) - \sum_{i=1}^{M} c_{p,i} \rho_i \mathbf{V}_i \cdot \nabla T - \sum_{i=1}^{M} h_i \omega_i.$$
 (2.11)

The equation above assumes that viscous heating is negligible on the account of the low speed of the fluid and that the pressure field p is spatially homogeneous, albeit varying in time. A mixture averaged model is employed for the thermal conductivity  $\Lambda$  (Mathur et~al.~1967). The specific enthalpy and the specific heat at constant pressure for species i are  $h_i = h_i(T)$  and  $c_{p,i} = c_{p,i}(T)$ , respectively, and are evaluated from NASA tables (McBride et~al.~1993).

Closure for the source terms  $\omega_i$  is provided by a chemical kinetics mechanism featuring 16 species and 73 elementary reactions of the Arrhenius type, which model the combustion of methane in air at 800 K and 4 atm accurately. More details on the kinetics mechanism and a comprehensive suite of validation cases are given in Luca *et al.* (2018*a*).

The configuration is a closed vessel of constant volume V, so that an ordinary differential equation for the evolution of the background pressure p(t) is obtained from the conservation of mass in the vessel:

$$p^{-1}\frac{dp}{dt} = -\left(\int_{V} \frac{W}{T} dV\right)^{-1} \frac{d}{dt} \int_{V} \frac{W}{T} dV. \tag{2.12}$$

#### 2.1. Numerical methods

Equations (2.1), (2.2), (2.5), and (2.11) are integrated in time with the finite difference solver "NGA" on a homogeneous Cartesian grid (Desjardins *et al.* 2008). The convective and viscous terms in the momentum equation and the diffusive terms in the scalar equations are discretized with second order centred finite difference formulas on a staggered grid. The third order Weighted Essentially Non-Oscillatory (WENO) scheme (Liu *et al.* 1994) is used for the convective terms in the scalar transport equations. Mass conservation

7

is enforced by solving a variable coefficients Poisson equation for the hydrodynamic pressure  $\pi$  instead of the continuity equation. The discrete form of the pressure equation is obtained with centred second order finite difference formulas.

The advancement in time of the governing equations follows a splitting approach (Tomboulides et al. 1997; Pierce 2001; MacArt & Mueller 2016). The momentum and pressure equations are coupled with the classic pressure-correction method (Chorin 1968). The momentum equation is integrated in time with a semi-implicit method featuring the explicit second order Adams-Bashforth method for the convective terms and the implicit Crank-Nicolson method for the linear viscous terms (Kim & Moin 1985). The linear system ensuing from the viscous terms is solved in factored form with the Alternating Direction Implicit (ADI) method (Peaceman & Rachford 1955). The time advancement of the temperature and mass fractions is performed with a first-order Lie splitting approach, whereby the integration of the convective and diffusive terms is performed first for each scalar field independently and that of the reactive source terms is handled at each grid point next. The temporal integration of the convective and diffusive terms is semi-implicit with the convective terms treated explicitly and the linear diffusive terms with the implicit Crank-Nicolson method and ADI factorization. The integration of the reactive source terms is performed point-wise with adaptive backward differentiation formula (BDF) methods as implemented in the CVODE solver for systems of ordinary differential equations (Hindmarsh et al. 2005).

The variable coefficients pressure equation is solved with the library HYPRE (Falgout et al. 2006) using the preconditioned conjugate gradient (PCG) iterative solver coupled with the parallel alternating semi-coarsening multi-grid V-cycle (PFMG) preconditioner. All governing equations are coupled together with an outer iteration loop and convergence is found to be adequate after two iterations (Pierce 2001).

The grid is homogeneous and isotropic with spacing  $\Delta=20~\mu\mathrm{m}$  and the time step size is constant at  $\Delta t=0.2~\mu\mathrm{s}$ . The spatial and temporal resolution are adequate, since  $\eta/\Delta \geqslant 0.5$  and  $\tau_{\eta}/\Delta t \geqslant 20$ , where  $\eta$  and  $\tau_{\eta}$  are the Kolmogorov length and time scale, respectively. Moreover,  $\delta_L/\Delta \geqslant 6$ , where  $\delta_L$  is the thermal thickness of the flame, as defined later in §3. Extensive numerical tests to confirm adequate spatial resolution for the reactive fronts were carried out for turbulent premixed jet flames (Luca *et al.* 2018*b*) and are not repeated here.

## 3. Flow configuration

The configuration consists of a cubic box filled with reactive mixture and initialized with homogeneous isotropic turbulence. A spherical kernel of burnt gases is initialized at the centre of the domain and a turbulent flame propagates outward into freely decaying turbulence. Periodic boundary conditions are imposed in all three directions, so that the computational domain represents a closed vessel. As burnt gases are produced behind the flame, the background pressure increases and the mixture is compressed isentropically. A schematic of the configuration is shown in figure 1.

The reactants are a fully premixed mixture of methane and air with equivalence ratio 0.7. At the onset of the simulation, the temperature and pressure are 800 K and 4 atm, respectively. At these thermo-chemical conditions, the laminar flame speed is  $S_L = 1 \text{ m s}^{-1}$ , the thermal thickness is  $\delta_L = (T_b - T_u)/\max\{|\nabla T|\} = 0.11 \text{ mm}$ , and the characteristic flame time  $\tau_L = \delta_L/S_L = 0.11 \text{ ms}$ . Here,  $T_b$  and  $T_u$  are the temperatures of the products and reactants, respectively, and  $\max\{|\nabla T|\}$  is the maximum value of the temperature gradient across the laminar flame.

In this study, a set of three primary simulations, denoted by R1, R2 and R3 are

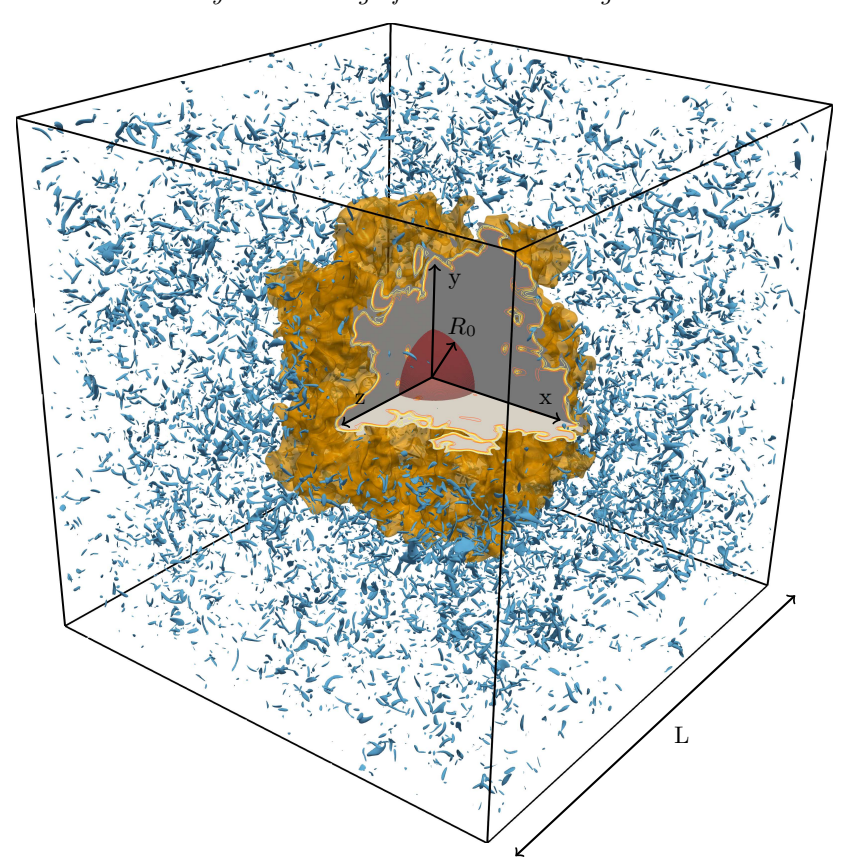


FIGURE 1. Turbulent spherical premixed flame in a cubic box of side L with periodic boundary conditions. The instantaneous flame surface (orange colour) is surrounded by homogeneous isotropic turbulence, represented by iso-surfaces of vorticity (blue colour). The flame surface corresponds to an iso-surface of the progress variable. The kernel of burnt gases at the onset of the simulation is shown as a sphere of radius  $R_0$  in the cut-out (red colour).

performed at increasing Reynolds number (see table 1). The Reynolds number is adjusted by varying the initial values of the fluctuation u' and integral scale l. Thus, the initial Reynolds number increases due to both u' and l increasing from R1 to R3. On the other hand, the Kolmogorov length scale  $\eta$ , velocity scale  $u_{\eta}$ , and time scale  $\tau_{\eta}$  are unchanged. Since the reactive mixture and associated flame scales  $S_L$ ,  $\delta_L$ , and  $\tau_L$  are unchanged also, this results in a constant initial Karlovitz number  $Ka = \tau_L/\tau_{\eta} = 25$  for all three simulations.

Turbulence decays freely as the flame front moves from the centre outwards. The statistical state of turbulence encountered by the propagating flame is characterized solely by the velocity fluctuation u', integral length scale  $l=u'^3/\epsilon$  based on the mean dissipation rate  $\epsilon$  of the turbulent kinetic energy k, and kinematic viscosity  $\nu$ , which all evolve in time. The eddy turnover time  $\tau=k/\epsilon$  is taken to represent a characteristic time for the motion of the largest scales. The relevant Reynolds number characterizing turbulence is  $Re_{\lambda}=u'\lambda/\nu$ , based on the transverse Taylor micro-scale  $\lambda^2=15\nu u'^2/\epsilon$  (Taylor 1935).

Unless otherwise noted, all characteristic scales of turbulence are evaluated with samples gathered in the volume occupied by the unburnt reactants only. Fluctuations are evaluated by subtracting the mean from the instantaneous field and the mean

Simulation	N	$2R_L/l_0$	$2R_0/l_0$	$R_L/R_0$	$u'/S_L$	$l_0/\delta_L$	$\delta_L/\eta$	$Re_{\lambda}$	Ka	$ au_0/ au_L$
R1	$512^{3}$	33.8	6.9	4.9	7.4	3.4	11.3	44	25	0.69
R2	$1024^{3}$	43.8	6.7	6.5	8.5	5.2	11.3	59	25	0.91
R3	$2048^{3}$	59.4	6.3	9.4	9.8	7.8	11.5	77	25	1.18
R3s	$1024^{3}$	29.7	6.3	4.7	9.8	7.8	11.5	77	25	1.18
R2a	$1024^{3}$	36.7	6.7	5.5	7.4	6.3	9.65	59	18	1.29

TABLE 1. Turbulence parameters at the onset of the simulations. N is the number of grid points. The effective domain radius  $R_L = (3/4\pi)^{1/3}L \approx 0.62L$  is defined based on L, the length of the side of the cubic domain. The flame properties are  $\delta_L = 0.11$  mm,  $S_L = 1$  m s<sup>-1</sup>, and  $\tau_L = 0.11$  ms. The Karlovitz number is defined as  $Ka = \tau_L/\tau_\eta$ .

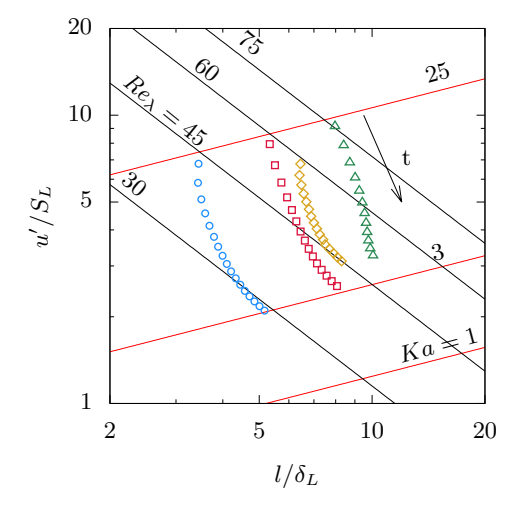


FIGURE 2. Instantaneous values of  $u'/S_L$  and  $l/\delta_L$  on the Borghi-Peters diagram of turbulent premixed combustion (Peters 2000): R1 ( $\bigcirc$ ), R2 ( $\bigcirc$ ), R2a ( $\diamond$ ), and R3 ( $\triangle$ ). The arrow points in the direction of increasing time. Also shown are lines of constant  $Re_{\lambda} = u'\lambda/\nu$  and Ka =  $\tau_L/\tau_{\eta}$ .

is obtained by ensemble averaging as appropriate (see §4.3). As turbulence decays freely while the flame propagates, the ratios  $u'/S_L$  and  $l/\delta_L$  vary in time as shown in figure 2. It is apparent that  $u'/S_L$  decreases as time progresses, while  $l/\delta_L$  increases slightly. The Karlovitz number decreases to  $Ka \approx 4$ . According to the Borghi-Peters classification (Peters 2000), all turbulent premixed flames belong to the flamelet regime.

The computational domain is a cube with side of length L. For reasons that will become clear later, we define the radius of a sphere, whose volume is equal to that of the cubic domain,  $R_L = (3/4\pi)^{1/3}L \approx 0.62L$ . It is apparent from table 1 that the size of the computational domain is large compared to the integral length scale. For example,  $2R_L/l \geqslant 30$  across all simulations. In particular, the extent of the domain is much larger than typically required for DNS of isothermal homogeneous isotropic turbulence at the same Reynolds number. Because the computational domain is large, the extent of the flame's surface may be initialized (and later grow to be) large compared to the integral length scale l. Although a rigorous quantitative definition will be given later in the article, the term "extent" refers to R, the average radial distance of the turbulent flame kernel from the centre of the domain. Since  $R \gg l$  throughout the evolution of the flame, the

flame is wrinkled by many eddies, the statistics are converged and spherically symmetric, and the flame remains centred in the middle of the domain (see §4.3).

The fact that the flame is large compared to the integral scale of the flow allows for motions over the entire turbulent spectrum to interact with the surface and affect its evolution. In other words, the entire spectrum of turbulence contributes to flame wrinkling, folding, and stretching. As articulated by Chaudhuri et al. (2011), if the integral scale were larger than the spherical flame, it is reasonable to expect that the flame's linear extent would act as a cut-off scale, limiting the interaction between the flame and turbulence to those scales smaller than the flame itself.

In keeping with the requirement that the initial flame kernel be large compared to the integral scale, the radius of the spherical kernel of burnt gases at the onset of the simulations  $R_0$  is rescaled to be consistent with l, so that the ratio  $2R_0/l \approx 7$  remains approximately constant across configurations.

When changing the Reynolds number of the flow, it is desirable to maintain as many dimensionless groups as possible constant in order to satisfy physical similarity (Buckingham 1914; Barenblatt 1996) and isolate the effect of scale separation as parametrized by the Reynolds number. In practice, compromises need to be made. For example,  $R_L/l$ , varies across simulations, although it is always large, as discussed. Similarly, the ratio  $R_L/R_0$ , which controls the extent of the pressure rise in the closed vessel, also varies across simulations, although the variation is inconsequential.

Two additional simulations, denoted by R2a and R3s, were conducted. Simulation R2a features the same initial Reynolds number as R2, but the fluctuation u' is lower, matching that of R1 and lowering the Karlovitz number. Comparisons between R1, R2a, and R2 help elucidate select aspects of the dependence of the turbulent burning rates on  $u'/S_L$ ,  $l/\delta_L$ , and  $Re_{\lambda}$ .

In order to investigate the effect of domain size on the propagation of the turbulent spherical premixed flame, simulation R3 was repeated with a domain of half the size and labelled R3s. Simulation R3s showed that the domain size  $R_L/l$  does not have any noticeable affect on the statistics pertaining to the evolution of the flame surface, although the size does affect the mean radial velocity induced by combustion (see §4.3).

## 3.1. Initial conditions and turbulence decay

The initial homogeneous isotropic turbulence (HIT) is generated as follows. First, preliminary HIT simulations at  $Re_{\lambda}$  are performed with the linear forcing scheme of Rosales & Meneveau (2005). Second, the velocity and dimensions are scaled to obtain the desired values of u' and l and several independent realizations of the velocity field are patched together into a larger domain. The motivation for patching boxes of homogeneous isotropic turbulence, rather than simulating fluid flow in the larger box, is due to a well known outcome of the forcing scheme, i.e. when a statistically stationary state is attained, the integral scale l is approximately 20% of the side of the cubic domain. Discontinuities in the velocity field across patches disappeared upon advancing the state over  $2\tau_n$ .

This patching strategy does not compromise the evolution of turbulence during decay as shown by previous studies (Albin 2010; Albin & DAngelo 2012). The kinetic energy spectra at different times during the isothermal decaying turbulence simulations conform to the expected Kolmogorov -5/3 scaling (see figure 3), but display a low value of the Kolmogorov constant  $C_k = E(k)e^{-2/3}\kappa^{5/3}$  in the small inertial range. Such differences are to be expected, since the value  $C_k = 1.5$  is observed only at high Reynolds numbers (Sreenivasan 1995).

Despite these differences in the Kolmogorov constant, all other turbulence statistics are consistent with the theory of decaying turbulence. In particular, the decay of the



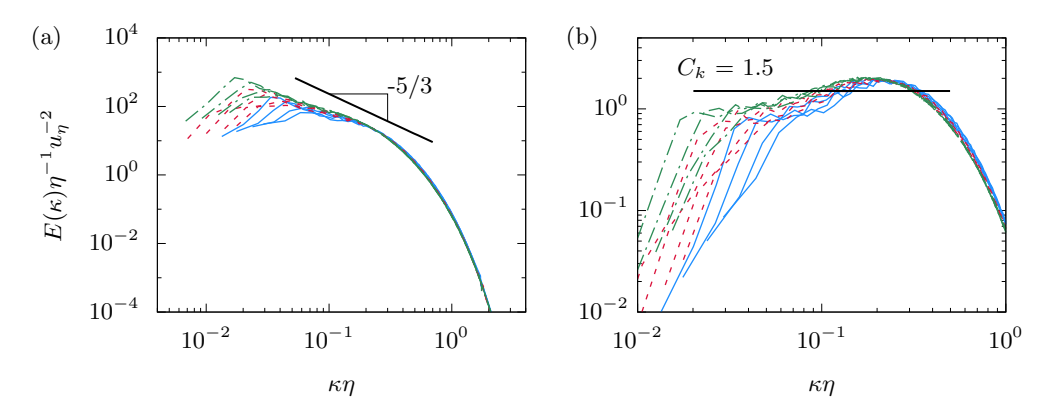


FIGURE 3. (a) Turbulent kinetic energy spectra at four instances (lines of same type and colour) during the decay of isothermal homogeneous isotropic turbulence for each of the three primary simulations: R1 (blue thin lines), R2 (red dashed lines), and R3 (green dot-dashed lines). (b) Compensated kinetic energy spectrum  $E(\kappa)\epsilon^{-2/3}\kappa^{5/3}$ . The thick solid line marks the Kolmogorov constant  $C_k = E(\kappa)\epsilon^{-2/3}\kappa^{5/3}$  for high Reynolds number flows (Sreenivasan 1995).

turbulent kinetic energy follows the power law (Batchelor & Townsend 1948a,b; Sinhuber et al. 2015),

$$k/k_0 = (1 + t/t_0)^{-n},$$
 (3.1)

where  $t_0$  is the virtual origin,  $k_0$  the turbulent kinetic energy at t = 0, and n is the decay exponent. The integral length scales of the flow evolves as

$$l/l_0 = (1 + t/t_0)^{1 - n/2}, (3.2)$$

where  $l_0$  denotes the integral scale at the onset of the simulations.

Experimentally, n is found to lie between 1 and 1.5. For decaying turbulence behind passive grids, Batchelor & Townsend (1948a) find n=1, Comte-Bellot & Corrsin (1971) report  $1.16 \le n \le 1.37$ , while Baines & Peterson (1951) find a higher value of n=1.43. Mohamed & Larue (1990) report that n=1.25 fitted their data best. Here, instead of fitting the parameters in (3.1) directly, we use the expression for the eddy turnover time

$$\tau = k/\epsilon = t_0/n(1 + t/t_0) = t_0/n + t/n, \tag{3.3}$$

so that n and  $t_0 = n\tau_0$  are related to the slope and intercept of a least-squares fit to  $\tau(t)$ . Figure 4(a) shows fits and power laws for  $k/k_0$  and  $\epsilon/\epsilon_0$ . In all simulations, we find n=1.55, which is slightly higher than the values reported in the literature. This discrepancy may be due to the low Reynolds number of our configurations or the dependence of the exponent on geometry, which differs between grid generated turbulence and simulations of homogeneous isotropic decaying turbulence.

Figure 4(d) compares the decay of Reynolds number in reactive and isothermal simulations from the same initial conditions. Statistics in the isothermal simulations are consistent with the power law decay, while in the reactive simulations, the changes in the background pressure and temperature cause minor deviations. While higher pressure and temperature lead to modifications to the density and the viscosity of the mixture, they are minor on the account of the fact that the maximum pressure rise is less than 20% across all simulations. Further, the differences at the end of the simulations are due in part to a decreasing number of samples available for statistics, since the unburnt gases occupy a region that decreases in volume as time progresses. We conclude that,



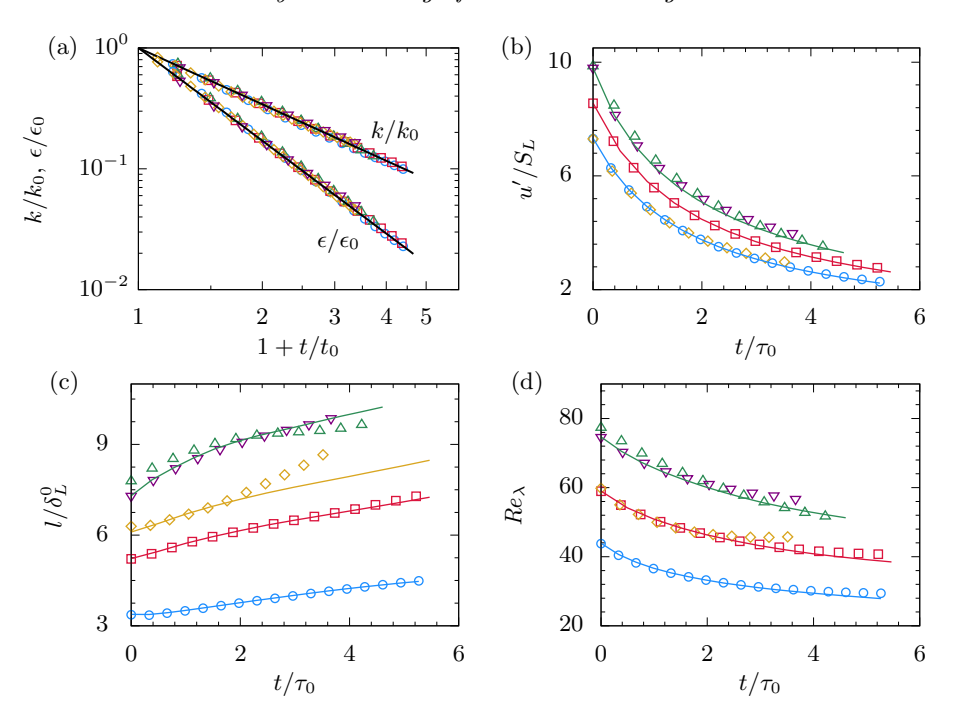


FIGURE 4. Statistics of the decaying turbulence in the reactants. (a) Exponential decay of turbulent kinetic energy  $k/k_0$  and its mean rate of dissipation  $\epsilon/\epsilon_0$  versus  $1+t/t_0$ , where  $t_0=n\tau_0$ . Lines represent power law expressions with n=1.55. Evolution of (b)  $u'/S_L$ , (c)  $l/\delta_L^0$ , and (d)  $Re_{\lambda}=u'\lambda/\nu$ . Lines represent decay in isothermal simulations, symbols represent data from reactive simulations: R1 ( $\bigcirc$ ), R2 ( $\square$ ), R2a ( $\diamond$ ), R3 ( $\triangle$ ), and R3s ( $\bigtriangledown$ ).

apart from minor differences that become more apparent at later times, the presence of a propagating flame does not change appreciably the decay of turbulence.

Finally, we notice that the data for simulations R3 and R3s prove that changes in the domain size do not have any noticeable effect on the statistics of decaying turbulence with or without a propagating flame.

## 4. Overview of the evolution of the turbulent premixed flames

#### 4.1. Basic definitions

Within the scope of the present study, the flame surface corresponds to an iso-surface of the reaction progress variable  $C(\mathbf{x},t) = c^*$ , which is defined as follows:

$$C = 1 - \frac{Y_{\mathcal{O}_2} - Y_{\mathcal{O}_2}^b}{Y_{\mathcal{O}_2}^u - Y_{\mathcal{O}_2}^b},\tag{4.1}$$

where  $Y_{\rm O_2}$  is the mass fraction of molecular oxygen and  $Y_{\rm O_2}^u$  and  $Y_{\rm O_2}^b$  are the mass fraction of oxygen in the reactants and products, respectively. By definition, the progress variable C increases monotonically from 0 in the reactants to 1 in the products. We let the isolevel  $c^*=0.73$  define the flame surface. This particular value of the progress variable corresponds to the maximum value of the heat release rate, which is taken to mark the middle of the reaction zone. The normal to the flame surface is defined as

$$\boldsymbol{n} = -\nabla C/|\nabla C|,\tag{4.2}$$

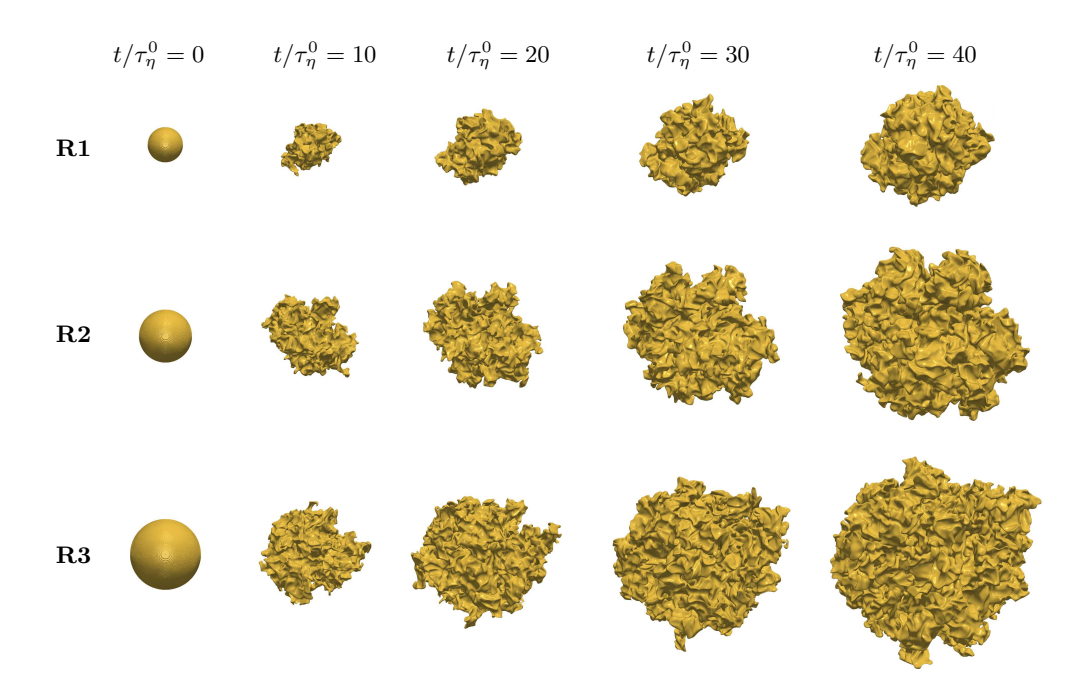


FIGURE 5. Instantaneous flame surface shown at various dimensionless times for the simulations R1, R2, and R3. The Reynolds number increases from top to bottom, while the simulation time increases from left to right. Since  $\tau_{\eta}^{0}$  is the same all three simulations, the flame surface is compared at the same physical time across simulations. The physical dimension is the same for all three flames also.

such that it points into the reactants. The flame propagates in the direction n with a displacement speed S relative to the local fluid velocity (Pope 1988; Chakraborty & Cant 2005)

$$S = \frac{1}{|\nabla C|} \frac{DC}{Dt} = \frac{1}{|\nabla C|} \left( \frac{\partial C}{\partial t} + \boldsymbol{u} \cdot \nabla C \right). \tag{4.3}$$

The displacement speed is computed from instantaneous numerical solutions as follows. The temporal derivative  $\partial C/\partial t$  is computed at the intermediate time  $t_{1/2} = t_n + \Delta t/2$  with a central finite difference formula based on two solutions at  $t_n$  and  $t_{n+1} = t_n + \Delta t$ . The velocity and scalar fields are interpolated linearly in time to  $t_{1/2}$ , the staggered velocity components are interpolated linearly onto the centred grid used for the progress variable scalar field, and a high-order central finite difference formula is used to evaluate the gradient of C.

## 4.2. The evolution of the turbulent premixed flames

Figure 5 illustrates the evolution of the turbulent spherical premixed flame during simulations R1, R2, and R3. The surface of the flame is visualized by the iso-surface  $C(\boldsymbol{x},t)=c^*$ , which marks the thin reaction zone of the flame. The flame, which is initialized as a spherical kernel of products centred in the middle of the computational domain, propagates radially outwards into the premixed reactants.

It is apparent that the flame surface is wrinkled and folded by turbulence as the flame propagates. Most patches of the flame surface are flat or posses only a slight curvature.

Regions of high curvature are much less prevalent and appear as sharp cylindrical folds, while cusps are infrequent. These qualitative observations are consistent with established topological features of the surface of turbulent premixed flames (Cifuentes et al. 2014). If the flames are compared at times when they are of similar size, the flame at the greatest value of the Reynolds number (R3) displays the highest density of folds and wrinkles. This is consistent with the qualitative interpretation that scale separation increases with increasing Reynolds number.

As reactants are converted into products inside the closed domain, the background pressure increases, leading to an increase in the reactants' temperature  $T_u$  also. The compression is isentropic. The simulations terminate when the mass fraction of burnt gases is less than 25% of the total, such that the effect of periodic boundary conditions is negligible. This ensures a small change in  $T_u$  ( $\leq 3\%$ ) and p ( $\leq 20\%$ ) for all simulations. We verified that such small changes in pressure and temperature lead to negligible changes in the laminar flame speed  $S_L$  ( $\leq 1\%$ ) and flame thickness  $\delta_L$  ( $\leq 10\%$ ).

## 4.3. Mean velocity field

Under the assumption of spherical symmetry of the mean fields, the Reynolds averaged continuity equation reads

$$\frac{\partial \langle \rho \rangle}{\partial t} + \frac{1}{r^2} \frac{\partial}{\partial r} r^2 \langle \rho u_r \rangle = 0, \tag{4.4}$$

where  $u_r = \mathbf{u} \cdot \mathbf{e}_r$  is the radial component of velocity and the term  $\langle \rho u_r \rangle$  is unclosed in general. In the regions occupied solely by reactants and products and away from the turbulent flame brush, density is spatially homogeneous and (4.4) simplifies to

$$\frac{1}{\rho} \frac{d\rho}{dt} + \frac{1}{r^2} \frac{\partial r^2 \langle u_r \rangle}{\partial r} = 0, \tag{4.5}$$

where  $\langle u_r \rangle$  is the mean radial component of velocity and the temporal variation of density is retained due to isentropic compression of the gases.

The isentropic relation  $\gamma d \ln \rho / dt = d \ln p / dt$ , where  $\gamma$  is the ratio of specific heats, is substituted into (4.5), which is then solved to give

$$\langle u_r \rangle = -\frac{1}{3\gamma} \frac{1}{p} \frac{dp}{dt} r + C_1 r^{-2}, \tag{4.6}$$

where  $C_1$  is a constant. In the region occupied by products,  $C_1 = 0$  since  $\langle u_r \rangle = 0$  at r = 0, yielding:

$$\langle u_r \rangle = -\frac{1}{3\gamma_b} \frac{1}{p} \frac{dp}{dt} r, \tag{4.7}$$

where  $\gamma_b$  is the ratio of specific heats of the burnt gases. (4.7) shows that  $\langle u_r \rangle$  is negative (dp/dt > 0) and varies linearly with r in the burnt gases.

At the domain boundary, the velocity is zero due to periodicity, but the boundaries' radial location depends on the polar  $(\Theta)$  and azimuthal  $(\Phi)$  angles on the account of the domain being a cube. Yet, since the mean radial velocity decreases as  $1/r^2$ , one expects the effect of geometry on the radial velocity to be negligible away from the boundary. Consequently, boundary conditions are imposed at an *effective* radial distance  $R_L$ , defined as the radius of a sphere with volume equal to that of the cubic domain

$$R_L = (3/4\pi)^{1/3}L. (4.8)$$

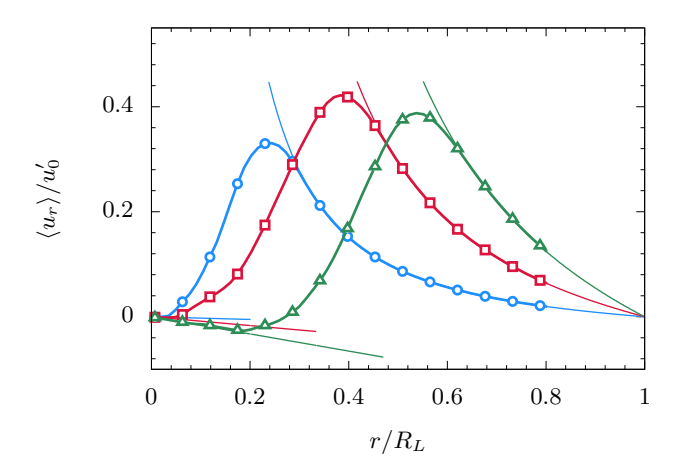


FIGURE 6. Reynolds averaged radial velocity  $\langle u_r \rangle$  normalized by the initial turbulence intensity for simulation R2. Data at three times:  $t/\tau_0 = 1.50$  ( $\bigcirc$ ), 3.35 ( $\square$ ), and 5.20 ( $\triangle$ ). Thin lines represent the expressions in (4.7) and (4.9) evaluated with the instantaneous value of  $p^{-1}dp/dt$ . Data for  $r/R_L \le 0.8$  ( $r/L \le 0.5$ ), which corresponds to the minimum distance from the centre to the boundary.

Then, the mean radial velocity component in the reactants reads

$$\langle u_r \rangle = -\frac{R_L}{3\gamma_u} \frac{1}{p} \frac{dp}{dt} \left[ \frac{r}{R_L} - \left( \frac{r}{R_L} \right)^{-2} \right], \tag{4.9}$$

where  $\gamma_u$  is the ratio of specific heats of the unburnt gases.

Figure 6 shows  $\langle u_r \rangle$  at three instants in time during the R2 simulation. The mean is obtained by ensemble averaging over  $\Theta$  and  $\Phi$ . The mean radial velocity matches the expressions in (4.9) and (4.7) closely at radial locations occupied by either products or reactants and away from the brush.

In particular, on the reactants' side, the theoretical expression for  $\langle u_r \rangle$  is identical to the data from the simulation up to r/L = 0.5 ( $r/R_L = 0.8$ ), which corresponds to the minimum distance between the centre and the faces of the cubic domain. We conclude that the mean flow retains spherical symmetry as if the computational domain were a spherical vessel with radius  $R_L$ . In the remainder of this article, turbulent statistics are assumed to be spherically symmetric and ensemble averaging is carried out accordingly.

## 4.4. Turbulent flame speed, area ratio, and correction factor

The relation between the linear extent of the flame, the flame's area and related fuel burning rate is of paramount importance to the understanding of the role of scale separation in turbulent premixed combustion applications. In this section, we introduce suitable statistical measures that facilitate our analysis and present an overview of their evolution across simulations.

The dimensionless turbulent flame speed  $S_T/S_L$  is the mean burning rate  $\Omega$  normalized by the fuel density in the reactants  $\rho_u Y_f$ , a reference area  $A^*$ , and the laminar flame speed  $S_L$ :

$$\frac{S_T}{S_L} = \frac{\Omega}{\rho_u Y_f S_L A^*}. (4.10)$$

Note that  $\Omega$  is defined here as the volumetric average of the rate of consumption of the

17

mass of the fuel in the domain. Further, divide and multiply the r.h.s. of (4.10) by the mean area of the flame surface A to obtain

$$\frac{S_T}{S_L} = \frac{\Omega}{\rho_u Y_f S_L A} \frac{A}{A^*}.$$
(4.11)

In the unsteady spherical flame configuration under study,  $\Omega = \Omega(t)$ ,  $\rho_u = \rho_u(t)$ , A = A(t), and we let  $A^* = 4\pi R^2$ , where R(t) is the mean flame radius.

In (4.11),  $\Omega$ , A, and  $A^*$  are time dependent statistical measures for which suitable estimators must be defined in a manner consistent with the ergodicity of the configuration. In other words, these quantities are neither random variables nor functions of random variables, rather they are statistics that vary in time due to the unsteadiness of the flow.

Both A and R are tied to the statistics of the progress variable field  $C(\mathbf{x},t)$ , since the flame surface is taken to coincide with the iso-surface  $C(\mathbf{x},t) = c^*$ . Formal definitions for the mean area A and mean radius R are given later in this Section.

As written, (4.11) shows that the normalized turbulent flame speed is equal to the product

$$\frac{S_T}{S_L} = \mathcal{I}\chi,\tag{4.12}$$

where  $\mathcal{I} = \Omega/(\rho_u Y_f S_L A)$  is the correction or stretch factor (Driscoll 2008) and  $\chi = A/A^*$  is the area ratio. There exists significant evidence in the literature that for turbulent flames under most circumstances of practical interest  $\mathcal{I} \approx 1$  and  $\chi \gg 1$ . In other words, the mean area of the turbulent flame is much greater than the reference area or  $A \gg A^*$ . If  $\mathcal{I} \approx 1$ , the ratio  $S_T/S_L$  is related to  $\chi$  alone and the mean burning rate may be written as

$$\Omega \approx \rho_u Y_f S_L A^* \chi. \tag{4.13}$$

While the practical value of (4.13) in scaling and estimating the mean burning rate  $\Omega$  is apparent, the dependence of the dimensionless area ratio  $\chi$  from all relevant non-dimensional groups, including the Reynolds and Karlovitz numbers among others, needs to be characterized for the flame configuration of interest.

When calculating  $S_T/S_L$ ,  $\chi$ , and  $\mathcal{I}$  from numerical simulations, the mean area of the flame surface A(t) is taken to be equal to  $\tilde{A}(t)$ , the area of the flame surface at time t during the simulation

$$\tilde{A}(t) = \int_{\mathcal{A}_c} d\mathcal{A},\tag{4.14}$$

where  $\mathcal{A}_c$  is the iso-surface  $C(\boldsymbol{x},t) = c^*$ , which represents the flame surface, and  $d\mathcal{A}$  is the area of its differential element. The mean flame radius is taken to be equal to the average of the distance function  $|\boldsymbol{x}|$  over the flame surface at time t

$$\tilde{R}(t) = \frac{1}{\tilde{A}(t)} \int_{\mathcal{A}_c} |\mathbf{x}| d\mathcal{A}. \tag{4.15}$$

Finally, the mean burning rate  $\Omega(t)$  is taken to be equal to the value of the burning rate  $\tilde{\Omega}(t)$ 

$$\tilde{\Omega}(t) = -\int_{V} \rho \dot{\omega}_{f} dV, \tag{4.16}$$

where  $CH_4$  is the fuel, so that  $\dot{\omega}_f = \dot{\omega}_{CH_4}$  and  $Y_f = Y_{CH_4}$ .

For the flame configuration considered, one instance of the turbulent flame at time t is found to be sufficient in order to estimate A, R, and  $\Omega$  from  $\tilde{A}$ ,  $\tilde{R}$ , and  $\tilde{\Omega}$ , respectively, and to characterize the variation of relevant statistics, including  $\chi$  and  $\mathcal{I}$ , in time and

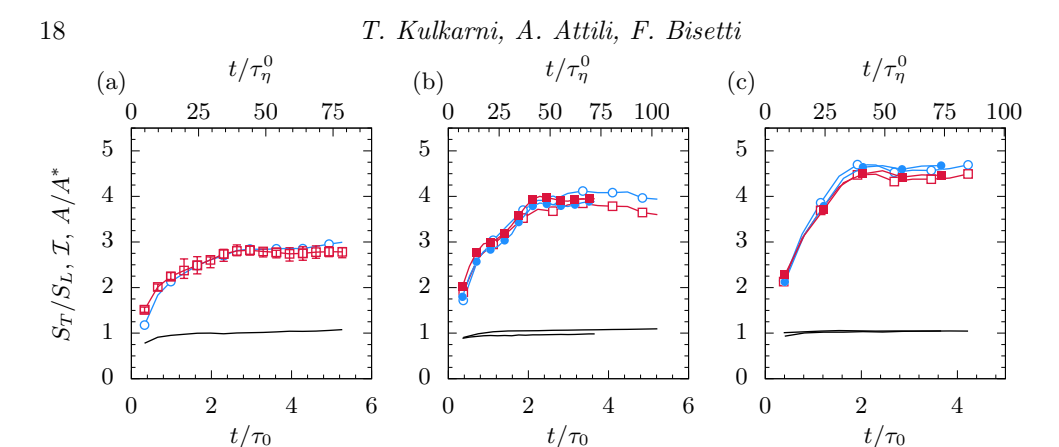


FIGURE 7. Dimensionless turbulent flame speed  $S_T/S_L$  ( $\bigcirc$ ), area ratio  $\chi$  ( $\square$ ), and correction factor  $\mathcal{I}$  (solid lines with no symbols). (a) R1 with error bars for the area ratio  $\chi$  representing the standard deviation across four simulations, (b) R2 (open symbols) and R2a (filled symbols) and (c) R3 (open symbols) and R3s (filled symbols).

across simulations. We explain this occurrence by noting that the configuration was designed so that the extent of the turbulent flame, characterized by its mean radius R, is large compared to the integral length scale of the flow. Because the surface area, radius, and burning rate are defined based on integrals over the polar and azimuthal angles, for which the flow fields display statistical symmetry, such arrangement provides multiple independent interactions of turbulence with the flame at any given time.

Convergence could be improved further by repeating each simulation multiple times and gathering several realizations of the same turbulent flow. Repeating each simulation was found to be computationally prohibitive, except for the R1 simulation, where the number of grid points was small enough to repeat the simulation four times with different initial conditions. In the rest of this article, all statistical quantities presented for simulations R2, R2a and R3 rely on one sample of the turbulent fields at each instant in time, while statistics for R1 rely on four independent realizations.

Figure 7 shows the temporal evolution of  $S_T/S_L$ ,  $\chi$ , and  $\mathcal{I}$  for the five simulations. Time is normalized by the eddy turnover time  $\tau_0$  on the primary axis, and by the Kolmogorov time  $\tau_\eta^0$  on the secondary independent axis, both calculated at the initial time. Since  $\tau_\eta^0$  does not vary for R1, R2, R3, and R3s,  $t/\tau_\eta^0$  is proportional to the dimensional time and allows comparisons across simulations.

It is apparent that  $\mathcal{I}$  is close to unity at all times, so that the normalized turbulent flame speed  $S_T/S_L$  is effectively equal to the area ratio  $A/A^*$ , which is greater than one. The temporal evolution of the area ratio is qualitatively similar across simulations, in that  $\chi$  grows rapidly and reaches a plateau afterwards. When measured in units of eddy turnover time  $\tau_0$ , the growth in  $\chi$  lasts approximately  $2\tau_0$  for all three simulations. In physical time units (or units of  $\tau_\eta^0$ ), the area ratio grows most rapidly for simulation R3. The asymptotic value reached by  $\chi$  for later times is smallest for R1 ( $\chi \to 2.8$ ) and largest for R3 ( $\chi \to 4.5$ ). Comparisons across R3 and R3s indicate that the size of the domain does not affect the burning rates. As discussed later, the same is observed for all other pertinent statistics.

The comparison of turbulent burning rates from R1, R2, and R2a points to the role of Reynolds number in controlling turbulent burning rates. R1 and R2a feature the same turbulence intensity  $u'/S_L$ , and yet R2a features higher burning rates than R1. On the other hand, simulations R2 and R2a share the same Reynolds number, differing in both

 $u'/S_L$  and  $l/\delta_L$ , yet they feature identical area ratios  $\chi$  when plotted versus  $t/\tau_0$ . More discussion on the Reynolds dependence of the area ratio is given in §6.

The remainder of this paper is concerned with the mechanisms responsible for the evolution of the area ratio  $A/A^*$  and its differences and similarities across simulations. The analysis is based on the formalism of the surface density function, which is discussed in §5.

## 5. The surface density function

#### 5.1. Basic definitions and mathematical framework

In order to quantify and explain the mechanisms responsible for the growth of the flame surface area and evolution of the area ratio, we adopt the formalism of the surface density function. The surface density function (SDF) is defined as the mean of the area of the flame surface per unit volume and is denoted by  $\Sigma$ . Note that  $\Sigma = \Sigma(r,t)$  is a statistical quantity, which depends on the radial coordinate r and time t for the present configuration.

The flame surface density of any iso-surface C(x,t) = c reads (Vervisch et al. 1995):

$$\Sigma(r,t;c) = \langle |\nabla C||C = c \rangle \mathcal{P}_C, \tag{5.1}$$

where  $\langle |\nabla C|| C = c \rangle$  is the conditional mean of the magnitude of the gradient of the progress variable and  $\mathcal{P}_C(C = c; r, t)$  is the probability density function (PDF) of C evaluated at the sample space value c. Although not noted explicitly, the conditional mean of  $|\nabla C|$  is a function of r and t in general. The SDF obeys the following transport equation (Vervisch et al. 1995):

$$\frac{\partial \Sigma}{\partial t} + \nabla \cdot (\langle \boldsymbol{u} + \boldsymbol{n} S \rangle_w \Sigma) = \langle K \rangle_w \Sigma. \tag{5.2}$$

In (5.2), S is the displacement speed as defined in (4.3),  $n = -\nabla C/|\nabla C|$  the normal to the flame surface pointing into the reactants, and K the flame stretch to be defined below.

The operator  $\langle \cdot \rangle_w$  denotes a conditional average weighted by the magnitude of the gradient of the progress variable:

$$\langle Q \rangle_w = \langle Q | \nabla C | | C = c \rangle / \langle | \nabla C | | C = c \rangle,$$
 (5.3)

where  $Q = Q(\boldsymbol{x}, t)$  is any random field. Such statistic is referred to as *surface average* (Pope 1988).

The source term on the r.h.s. of (5.2) represents the surface average of stretch K:

$$K = a - 2S\kappa. (5.4)$$

The first term is hydrodynamic in nature

$$a = -n\nabla u n + \nabla \cdot u, \tag{5.5}$$

where a is the tangential strain rate, which depends solely on the velocity field u and the orientation of the velocity gradient tensor  $\nabla u$  with respect to the flame normal n. The second term consists of the product of the mean flame curvature  $\kappa$  and displacement speed S

$$-2S\kappa = S\nabla \cdot \boldsymbol{n}.\tag{5.6}$$

This term is referred to as the *propagative term* or the *curvature term* as it is non-zero only for surfaces that propagate  $(S \neq 0)$  in the presence of curvature  $(\kappa \neq 0)$ . In the

case of a material surface, K = a and surface stretch is due to tangential strain only. Recall that a material surface is associated with a scalar field for which both diffusion and reactions are absent.

By definition of the surface density function, the mean surface area A is the volumetric integral of the surface density function for  $C = c^*$ ,

$$A(t) = 4\pi \int_0^\infty r^2 \Sigma(r, t) dr, \qquad (5.7)$$

where  $C = c^*$  is the iso-surface that identifies the flame front as outlined earlier. Note that the mean area in (5.7) depends on time only since the radial dependence of the SDF is lost in the integration.

Again, the surface density function is a statistical quantity estimated here based on a single realization of the turbulent flow, exploiting the ergodicity of the flow with respect to the polar and azimuthal angles. Convergence of simulation R1 is further improved by using four independent realizations. The definitions of A in (4.14) and (5.7) are mathematically equivalent (Maz'ja 1985) and less than 1% difference between the two is observed when they directly computed directly from DNS data in all cases.

The evolution equation for the flame surface area is readily obtained by volumetric integration of (5.2)

$$\frac{dA}{dt} = \frac{d}{dt} \int_{V} \Sigma \, dV = -4\pi \int_{0}^{\infty} \frac{d}{dr} (\langle u_r + S n_r \rangle_w \Sigma) \, dr + 4\pi \int_{0}^{\infty} r^2 \langle K \rangle_w \Sigma \, dr. \tag{5.8}$$

The first term on the right hand side of (5.8) is zero since  $\Sigma$  goes to zero at both extremes of integration. Then, the global stretch, defined as the logarithmic time derivative of the surface area A, is written as

$$K_G = (1/A) dA/dt = \int_0^\infty r^2 \Sigma \langle K \rangle_w dr \left( \int_0^\infty r^2 \Sigma dr \right)^{-1}.$$
 (5.9)

Finally, the area ratio  $\chi$  is expressed in terms of  $\Sigma$  as

$$\chi(t) = \int_0^\infty (r/R)^2 \Sigma(r,t) dr.$$
 (5.10)

#### 5.2. PDF of radial distance of the flame surface

We now consider the probability density function associated with the distance of the flame surface, which is denoted by  $\mathcal{P}_{\phi}$ . Here  $\phi$  is the random variable representing the distance of the flame surface from the origin. With this formalism, the mean flame radius R and the thickness of turbulent brush  $\delta$  are defined as moments of  $\mathcal{P}_{\phi}$  and their governing equations derived from the SDF transport equation. This points to the importance of the flame radial distance PDF in analysing the evolution of the area ratio.

The mean area the surface inside the sphere of radius  $\varphi$  is

$$A_{\varphi} = 4\pi \int_{0}^{\varphi} r^{2} \Sigma(r, t) dr, \qquad (5.11)$$

so that the ratio  $A_{\varphi}/A$  represents the probability  $\mathbb{P}(\phi < \varphi)$  and describes the cumulative density function associated with  $\mathcal{P}_{\phi}$ . The PDF is obtained by differentiation with respect to the sample space variable  $\varphi$ 

$$\mathcal{P}_{\phi}(\phi = \varphi; t) = d(A_{\varphi}/A)/d\varphi = 4\pi A^{-1} \varphi^{2} \Sigma(r = \varphi, t), \tag{5.12}$$

with support  $\varphi \in [0, \infty)$ . In light of (5.12), the rate of change of  $\mathcal{P}_{\phi}$  reads

$$\partial \mathcal{P}_{\phi}/\partial t = \left(4\pi r^2/A\right) \left\{\partial \Sigma/\partial t - (\Sigma/A) \, dA/dt\right\}. \tag{5.13}$$

21

Substituting  $\partial \Sigma/\partial t$  from (5.2) and  $K_G$  from (5.9) into (5.13), we obtain

$$\partial \mathcal{P}_{\phi}/\partial t = -\partial/\partial r \left\{ \langle u_r + S n_r \rangle_w \mathcal{P}_{\phi} \right\} + (\langle K \rangle_w - K_G) \mathcal{P}_{\phi}. \tag{5.14}$$

The mean  $\mu$  and standard deviation  $\sigma$  of  $\phi$  are the mean radial distance and a scaled flame brush thickness  $\sigma = \delta/\sqrt{2\pi}$ :

$$R \equiv \langle \phi \rangle = \int_0^\infty \varphi \mathcal{P}_\phi(\varphi; t) \, d\varphi$$
$$= 4\pi A^{-1} \int_0^\infty r^3 \Sigma(r, t) \, dr \tag{5.15}$$

and

$$\sigma^{2} = \langle (\phi - \langle \phi \rangle)^{2} \rangle = \int_{0}^{\infty} (\varphi - \langle \phi \rangle)^{2} \mathcal{P}_{\phi}(\varphi; t) \, d\varphi$$
$$= 4\pi A^{-1} \int_{0}^{\infty} (r - R)^{2} r^{2} \Sigma(r, t) \, dr. \tag{5.16}$$

With the above definition,

$$\delta = \sqrt{2\pi}\sigma = 1/\max\{d\langle C\rangle/dr\},\tag{5.17}$$

where  $\langle C \rangle (r,t)$  is the mean progress variable and  $d \langle C \rangle / dr$  its gradient under the hypothesis of spherical symmetry. The two definitions of the brush thickness are equivalent under the assumption that the surface is normally distributed around the mean location (e.g. see Chp. 4 in Lipatnikov 2012).

## 5.3. Characterization of $\mathcal{P}_{\phi}$ and $\Sigma$

The mathematical framework in §5.1 and §5.2 demonstrates that the mean area A, mean radius R, turbulent flame brush  $\delta$ , and area ratio  $\chi$  are related functionally to the surface density function  $\Sigma$ . Further, (5.12) points to an equivalence between  $\Sigma$  and the probability density function  $\mathcal{P}_{\phi}$ .

The evolution of the first two moments of  $\mathcal{P}_{\phi}$  is shown in figure 8. The flame radius is normalized by the radius of the initial spherical kernel,  $R_0$ , while the brush is normalized by the initial integral length scale,  $l_0$ . Time is normalized by  $\tau_0$ , the eddy turnover time at the onset of each simulation (see table 1).

It is apparent that the evolution of  $R/R_0$  is similar across simulations and that each simulation lasts about 4 to 5 eddy turnover times. During this time, the flame radius changes by a factor of 2.5 (R1) to 3 (R2 and R3). The data illustrate that there are two phases in the evolution of the flame radius. Early on, the radius increases slowly, yet its growth rate increases steadily, while later R grows linearly in time. Although the temporal evolution of  $R/R_0$  does not collapse across simulations when plotted against  $t/\tau_0$ , these data do show that the onset of this second phase of linear growth occurs at  $t/\tau_0 \approx 1$  for all configurations and that the non-dimensional growth rate  $R_0^{-1}\tau_0 dR/dt$  differs, being greatest for R3 and smallest for R1.

The flame brush  $\delta/l_0$  increases monotonically in time across simulations as shown in figure 8(b) and similar across simulations, which is a result of the scaling of the flame brush thickness with the integral length scale of the flow as discussed later in §6.1.

The PDF  $\mathcal{P}_{\phi}$  can be closely approximated by a Gaussian distribution. This is demonstrated in figure 9, which shows  $\mathcal{P}_{\phi}$  at four times for three simulations. Here we plot the

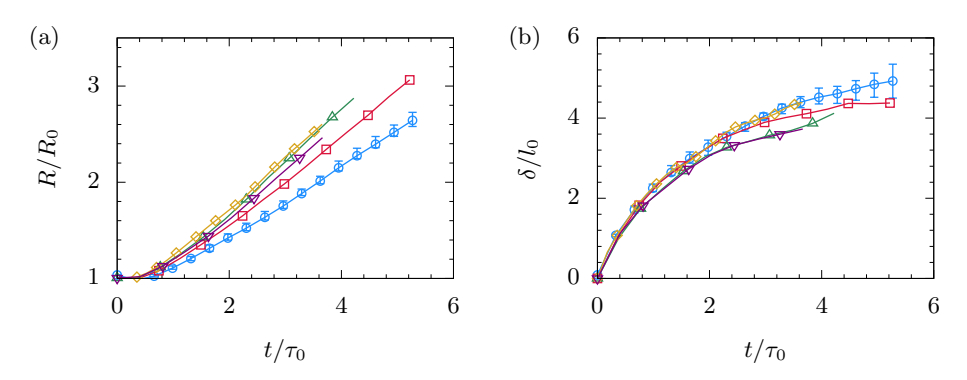


FIGURE 8. Evolution of (a) mean flame radius and (b) flame brush thickness for various simulations. The mean flame radius is normalized by the initial kernel size  $R_0$ , while the brush thickness is normalized with the initial integral length scale  $l_0$ : R1 ( $\bigcirc$ ), R2 ( $\square$ ), R2a ( $\diamond$ ), R3 ( $\triangle$ ), and R3s ( $\triangledown$ ). Error-bars shown for R1 simulation are based on four different realizations.

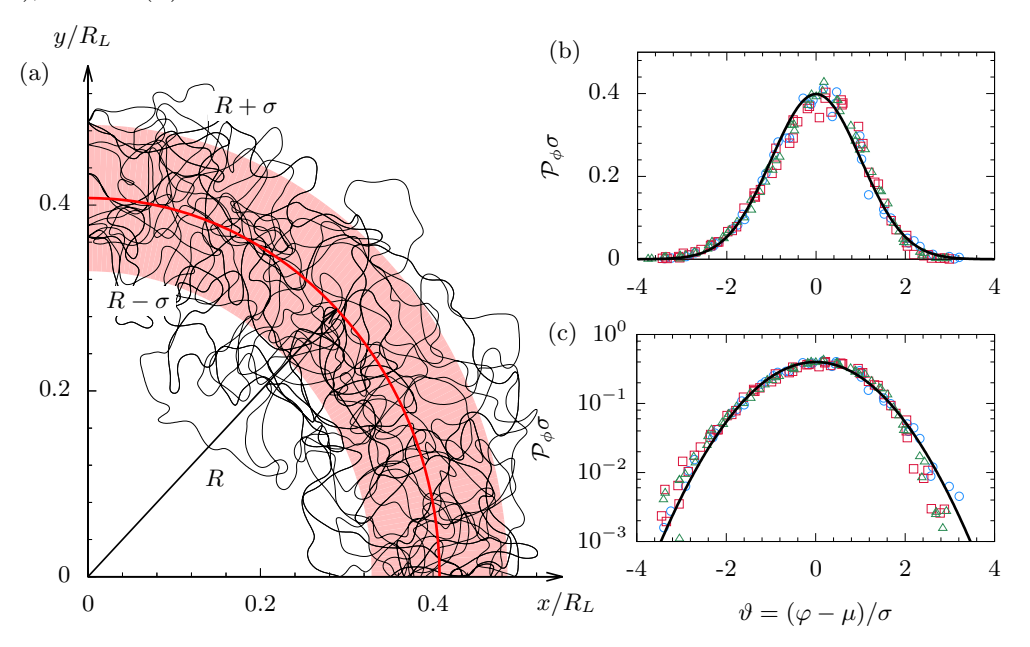


FIGURE 9. (a) Planar slices of the instantaneous flame surface for simulation R2 at  $t/\tau_0 = 4.2$ . The mean flame radius (thick red line) and several  $C = c^*$  iso-contours (thin black lines) are shown alonside the shaded region  $r = R \pm \sigma$ . Also shown in (b) and (c) is the  $\sigma \mathcal{P}_{\phi}$  at four times for simulations R1 ( $\bigcirc$ ), R2 ( $\square$ ) and R3 ( $\triangle$ ) with the standard normal distribution for comparison (thick black lines).

PDF normalized by  $\sigma$  and against  $\vartheta$ , a sample space variable of the normalized brush coordinate  $\theta = (\phi - \mu)/\sigma$ . It is apparent that  $\sigma \mathcal{P}_{\phi}$  is well described by a standard normal distribution  $\mathcal{N}(0,1)$ , consistently with previous data reported in the literature for various flame configurations (Lipatnikov & Chomiak 2002). The inset shows that the tails of the PDF are also well approximated by the normal distribution, although the comparison becomes less satisfactory for  $|\vartheta| > 2$ , possibly due to statistical convergence.

Figure 10 shows  $\Sigma$  at select times for simulations R1, R2, R3, and R2a. The SDF is shown normalized by the initial thermal thickness  $\delta_L^0$  and plotted versus  $r/R_L$ , where  $R_L$  is the effective domain radius (see table 1). The surface density distribution is

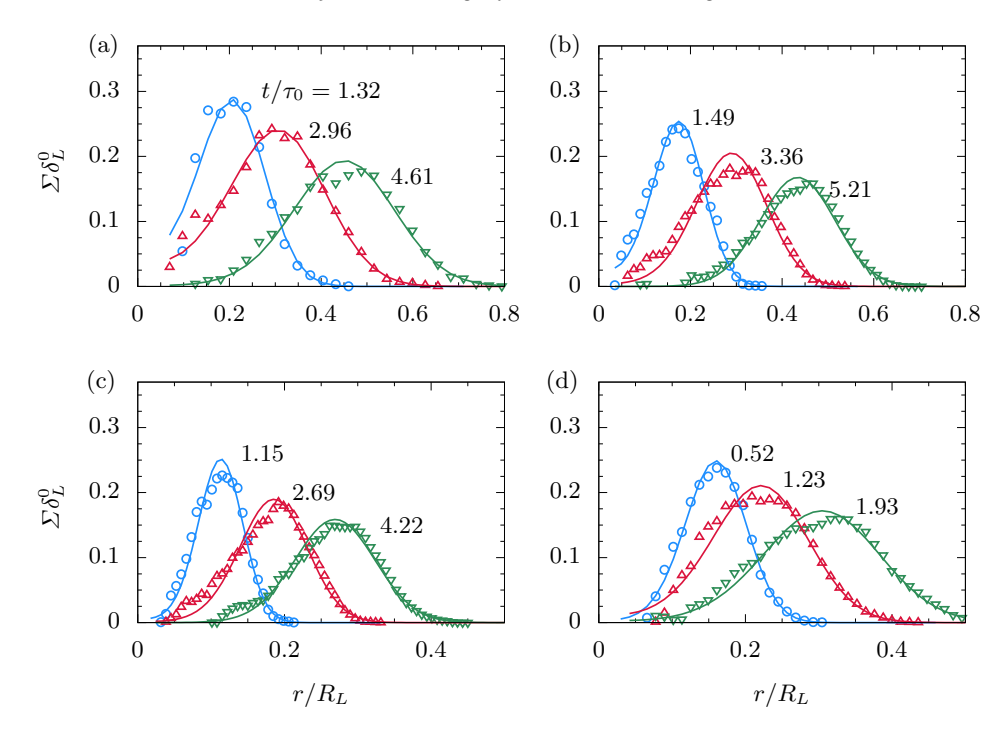


FIGURE 10. Surface density function at select times for (a) R1, (b) R2 (c) R3, and (d) R2a. The normalized time  $t/\tau_0$  is shown next to each profile. The surface density distribution broadens and the peak reduces as the time progresses. Symbols denote evaluation of  $\Sigma$  using (5.1) directly, while solid lines show surface density estimation based on (5.12) and a normal distribution model for  $\mathcal{P}_{\phi}$ .

transported radially outward, broadens, and its maximum value  $\Sigma_m$  decreases with time. This behaviour is common across all cases. The broadening of  $\Sigma$  is consistent with the increase in the flame brush and with experimental observations of spherical turbulent premixed flames evolving in freely decaying turbulence (Renou et al. 2002; Fries et al. 2019). Since the area ratio  $\chi$  is related to the volumetric integral of  $\Sigma$ , broadening appears to be closely related to the observed increase of  $\chi$  in time. Yet, the peak of  $\Sigma$  decreases in time, so that a more quantitative analysis is in order.

Using a Gaussian distribution as a model for  $\mathcal{P}_{\phi}$ , the surface density function is obtained according to (5.12) and shown in figure 10 also.  $\Sigma$  obtained assuming that  $\mathcal{P}_{\phi}$ is a normal distribution is compared to its direct evaluation as in (5.1). The comparison is very satisfactory, indicating that the two methodologies are consistent and further validating our approach. Nonetheless,  $\Sigma$  computed from conditional statistics displays residual statistical noise, and therefore we rely on the model to analyse the peak value of the surface density function.

## 5.4. Model for the area ratio

We begin by noting that the surface density function admits a local maximum at radial location  $\hat{r}$ , which is the root of the equation

$$\frac{\partial \Sigma}{\partial r}\Big|_{r=\hat{r}} = -2\mathcal{P}_{\phi}(\hat{r})/\hat{r}^3 + \mathcal{P}'_{\phi}(\hat{r})/\hat{r}^2 = 0$$

$$2\mathcal{P}_{\phi}(\hat{r}) - \hat{r}\mathcal{P}'_{\phi}(\hat{r}) = 0,$$
(5.18)

$$2\mathcal{P}_{\phi}(\hat{r}) - \hat{r}\mathcal{P}_{\phi}'(\hat{r}) = 0, \tag{5.19}$$

where we let  $\mathcal{P}'_{\phi}$  indicate the derivative with respect to  $\varphi$ . Based on (5.12), the maximum value attained by the surface density function is

$$\Sigma_m \equiv \Sigma(\hat{r}, t) = (4\pi)^{-1} A \frac{\mathcal{P}'_{\phi}(\hat{r})}{2\hat{r}} = (4\pi)^{-1} A \frac{\mathcal{P}_{\phi}(\hat{r})}{\hat{r}^2}.$$
 (5.20)

Substitution of (5.12) and (5.20) into (5.10) gives

$$\chi = \Sigma_m \delta \beta, \tag{5.21}$$

where

$$\beta = \frac{1}{\mathcal{P}_{\phi}(\hat{r})\delta} \left(\frac{\hat{r}}{R}\right)^2 \tag{5.22}$$

is a shape factor related solely to the functional form of  $\mathcal{P}_{\phi}(\varphi;t)$ . Equation (5.21) illustrates that the area ratio  $\chi$  is proportional to the product of the maximum value of the surface density function, the thickness of the flame brush, and a shape factor.

As shown in figure 9,  $\mathcal{P}_{\phi}(\varphi;t)$  is well approximated by a normal distribution. On the account that  $\mathcal{P}_{\phi}$  is defined in  $[0,\infty)$ , a truncated normal distribution with parameters  $\bar{\mu}$  and  $\bar{\sigma}^2$  (Johnson *et al.* 1994) is required formally, rather than a normal distribution with infinite support  $\varphi \in (-\infty,\infty)$ . However, we find that for all simulations,  $\bar{\mu} \geqslant 3\bar{\sigma}$  (see figure 9), so that  $\bar{\mu} \approx \mu$ ,  $\bar{\sigma}^2 \approx \sigma^2$ , and the normalization factor  $Z = 1 - F(-\bar{\mu}/\bar{\sigma}) \approx 1$ , where F(z) is the cumulative distribution function of the standard normal distribution.

Thus, for all practical purposes, the truncated normal distribution and the underlying normal distribution are identical on the account of the negligible probability of  $\phi$  taking negative values. For simplicity, we ignore the small differences arising from the truncated sample space at  $\varphi = 0$  and model  $\mathcal{P}_{\phi}$  as a normal distribution with parameters  $\mu = R$  and  $\sigma^2 = \delta^2/(2\pi)$ . This results in the following root of (5.19)

$$\hat{r} = 2\mathcal{P}_{\phi}(\hat{r})/\mathcal{P}'_{\phi}(\hat{r}) = R\left(1 + \sqrt{1 - 8\alpha^2}\right)/2,$$
 (5.23)

where  $\alpha = \sigma/\mu$  ( $\alpha \le 0.33$  for all times and simulations) is the relative standard deviation of the radial distance. Substituting (5.23) into (5.22), the shape factor reads

$$\beta = \beta(\alpha) = 0.25 (1 + \sqrt{1 - 8\alpha^2})^2 \exp\left\{\alpha^2 (\sqrt{1 - 8\alpha^2} - 1)^2 / 8\right\}.$$
 (5.24)

Equation (5.24) indicates that the shape factor is a monotonic function of  $\alpha$ . For  $\alpha \to 0$ ,  $\beta \to 1$  and decreases as  $\alpha$  increases. For all simulations and times, we find  $0.875 \le \beta \le 1$ .

Together with the fact that  $\beta \approx 1$ , (5.21) illustrates that the area ratio  $\chi$  is equal to the product of the maximum value of the surface density function  $\Sigma_m$  and the thickness of the flame brush  $\delta$ . In particular, the temporal evolution of these two quantities across simulations with varying Reynolds number is explored closely.

## 6. Scaling of the area ratio in spherical turbulent premixed flames

6.1. Scaling of the turbulent flame brush thickness

As defined in (5.17), the flame brush thickness  $\delta(t)$  is a statistical measure of the distance of the flame surface from its mean location. The brush thickness grows from zero as time progresses and turbulence wrinkles the flame (figure 8(b)).

Under rather stringent assumptions and important approximations, Taylor's theory of turbulent diffusion has been applied to the evolution of the flame brush thickness (Lipatnikov & Chomiak 2002). First, the flame surface is assumed to evolve as

a collection of infinitesimal material surface elements and the variance of the distance of the surface elements from their mean location is taken to represent the brush thickness. Second, turbulence is assumed to be homogeneous and isotropic, although not necessarily stationary. Under these assumptions, the rate of change of the variance of the distance is

$$d\sigma^{2}/dt = 2u'(t) \int_{0}^{t} u'(p) f_{L}(p,t) dp,$$
(6.1)

where  $f_L$  denotes the Lagrangian velocity autocorrelation function and u'(t) is the turbulence intensity at time t. For stationary turbulence, (6.1) is integrated assuming that the autocorrelation function is exponential (Hinze 1975) to give

$$\sigma^2/l^2 = 2\tilde{t}\{1 - \tilde{t}^{-1}[1 - \exp(-\tilde{t})]\},\tag{6.2}$$

where  $\tilde{t} = t/\tau^{\dagger}$  and  $\tau^{\dagger} = l/u'$  is a constant reference time scale. The short and long time behaviours described by (6.2) are  $\sigma^2 \sim t^2$  for  $t \ll \tau^{\dagger}$  and  $\sigma^2 \sim t$  for  $t \gg \tau^{\dagger}$ , respectively.

The short time limit has been shown to explain reasonably well the early and near-field evolution of the brush for various experimental and numerical flame configurations, including spherically expanding flames and turbulent Bunsen flames (Lipatnikov & Chomiak 2002). For spatially inhomogeneous turbulent flows with a dominant direction, a convective time related to distance is used in place of time. This model suggests that the flame brush thickness scales with large, energy containing scales of turbulence, since the ratio  $\sigma/l$  is a function of the normalized time  $t/\tau^{\dagger}$  alone.

Minor adjustments to (6.1) and (6.2) are required for spherical expanding flames in decaying turbulence. Firstly, the brush thickness is defined in terms of the variance of the radial distance, so that only the radial component of the velocity vector along the Lagrangian trajectories should be considered. Since the radial direction varies along a Lagrangian trajectory, the integrand includes an orientation factor also and reads

$$d\sigma^2/dt = 2u'(t) \int_0^t u'(p) f_L(p,t) \langle \cos \alpha_{p,t} \rangle dp, \tag{6.3}$$

where  $\langle \cos \alpha_{p,t} \rangle$  is the expectation of  $\alpha_{p,t}$ , the angle between two position vectors on a Lagrangian trajectory at times p and t. The derivation of (6.3) is presented in Appendix A.

Since  $\cos \alpha_{p,t} \leq 1$ , (6.1) over-estimates the rate of change of the brush thickness compared to (6.3). Nonetheless, the correction is small if the lateral movement on a Lagrangian trajectory during temporal intervals for which the velocity remains correlated is small compared to the radial distance of the material point. A comprehensive analysis of the correction factor requires an investigation of Lagrangian statistics and is outside the scope of the present study. Thus, we interpret (6.1) as an *upper bound* on the rate of change of the brush thickness in spherically expanding flames as approximated by Taylor's theory of turbulent diffusion.

A second aspect is related to the fact that turbulence in not stationary, rather it decays in time. Batchelor & Townsend (1956) postulated that the Lagrangian velocity autocorrelation in decaying isotropic turbulence is self-similar and argued that, if the decay of the turbulent kinetic energy follows a power law (see §3.1), there exits a characteristic time scale  $\tau_s$  for which  $u(t)(1+t/t_0)^{-n/2}$  is a stationary random variable in the transformed time coordinate s, defined so that  $ds = dt/\tau_s$ . Batchelor & Townsend (1956) suggested  $\tau_s = t + t_0$ , which was supported later by Huang & Leonard (1995) based on a model spectrum of the Lagrangian velocity autocorrelation at high Reynolds numbers. Letting  $s = \log(1+t/t_0)$  with  $t_0 = n\tau_0$ , all length and velocity scales in decaying turbulence are exponential functions of s. Further, as shown by Huang & Leonard (1995),

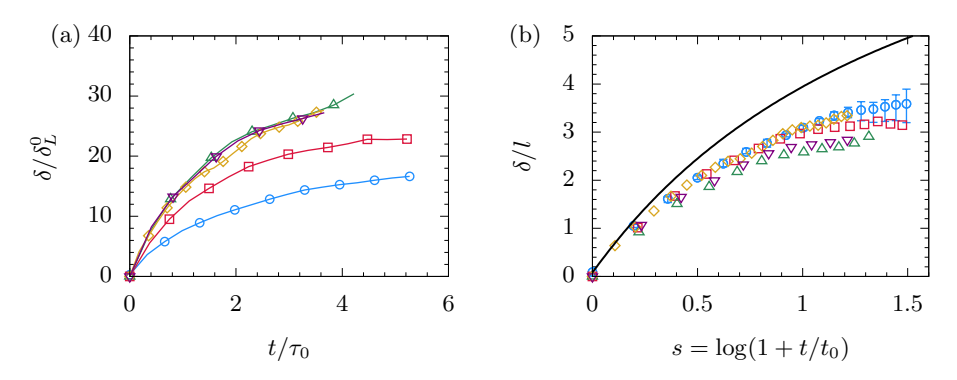


FIGURE 11. Temporal evolution of the flame brush thickness. (a) Brush thickness normalized by the thermal thickness of the laminar flame,  $\delta_L^0$ , versus time normalized by the initial eddy turnover time. (b) Normalized flame brush thickness  $\delta/l$  versus the transformed time coordinate  $s = \log(1 + t/t_0)$ , where  $t_0 = n\tau_0$ . The solid line shows the expression in (6.4). Symbols identify data from different simulations: R1 ( $\bigcirc$ ), R2 ( $\bigcirc$ ), R2a ( $\diamond$ ), R3 ( $\bigcirc$ ), and R3s ( $\bigcirc$ ).

the Lagrangian autocorrelation function depends on the lag between two transformed time coordinates, i.e.  $f_L(t_1, t_2) = f_L(s_1 - s_2)$ . The methodology for the estimation of the parameters  $t_0$  and n was outlined in §3.1.

Substituting the expressions for the turbulent kinetic energy (3.1) and eddy turnover time (3.3), the temporal evolution of  $\delta^2$  reads

$$\delta^2/l^2 = (9\pi n^2) \int_0^s dp \int_0^p dq \, f_L(q-p) \exp\{(1-n/2)(p+q-2s)\}.$$
 (6.4)

The factor in front of the integral in the above expression originates from the definition of the eddy turnover time  $\tau = 3l/2u' = 3\tau^{\dagger}/2$  and  $\tau_s = n\tau$ . Equation (6.4) suggests that  $\delta/l = f(s)$  alone and that the *instantaneous* integral length scale of the flow l is the obvious length to normalize the brush thickness  $\delta$ .

Figure 11 shows the temporal evolution of the normalized flame brush  $\delta/l$  for all simulations alongside the theoretical prediction from (6.4). The expression for the Lagrangian autocorrelation function given in Huang & Leonard (1995) was used to evaluate the integrals on the r.h.s. of (6.4).

Consistent with the observations in the literature, we report good agreement of the brush thickness with the theory of turbulent diffusion early on  $(s < 0.2 \text{ or } t/\tau_0 < 0.5)$  and a near collapse across simulations. This agreement is rather remarkable considering that the flame surface is defined based on the iso-surface of a reactive scalar and propagates in a variable density and variable properties flow, while Taylor's theory of turbulent diffusion applies to an ensemble of material points convected by an isothermal fluid. Nonetheless, the agreement is best at early times and deviations from theory are apparent later. More importantly, the evolution of  $\delta/l$  appears to saturate towards a limit value, while theory predicts continuous growth even in decaying turbulence.

To investigate the deviations from the turbulent diffusion theory, we consider the evolution equation for the brush, which is derived next. Despite the deviations, the scaling of  $\delta$  with l is robust, as the evolution of  $\delta/l$  is nearly the same across different simulations.

#### 6.1.1. Evolution equation for turbulent brush thickness

The evolution equation for the flame brush thickness is readily obtained by taking the second central moment of (5.14) and reads

$$\frac{d\delta^2}{dt} = 4\pi \int_0^\infty \langle u_r + S n_r \rangle_w (r - R) \mathcal{P}_\phi \, dr + 2\pi \int_0^\infty \langle K' \rangle_w (r - R)^2 \mathcal{P}_\phi \, dr, \tag{6.5}$$

where  $K' = K - K_G$  is the differential stretch rate. The first term on the r.h.s of (6.5) describes the effect of transport on the brush and consists of contributions by the mean radial velocity, velocity fluctuations, and flame propagation.

We decompose the radial velocity as  $u_r = \langle u_r \rangle + u_r'$ , where  $\langle u_r \rangle$  is the *unconditional* Reynolds average, so that  $\langle u_r' \rangle_w$  is not zero, and the evolution equation is manipulated to read:

$$\frac{d\delta}{dt} = (2\pi/\delta) \int_0^\infty \langle u_r' \rangle_w (r - R) \mathcal{P}_\phi \, dr + (2\pi/\delta) \int_0^\infty \langle u_r \rangle (r - R) \mathcal{P}_\phi \, dr 
+ (2\pi/\delta) \int_0^\infty \langle S n_r \rangle_w (r - R) \mathcal{P}_\phi \, dr + (\pi/\delta) \int_0^\infty \langle K' \rangle_w (r - R)^2 \mathcal{P}_\phi \, dr.$$
(6.6)

In the order in which they appear on the r.h.s. of (6.6), the terms represent contributions from velocity fluctuations or turbulent transport (term I), transport due to mean radial velocity (term II) and flame propagation (term III), and differential stretch (term IV).

Figure 12 shows  $d\delta/dt$  and the four terms on the right hand side of (6.6). All terms are normalized by the initial turbulence intensity  $u_0'$ . The rate of change of  $\delta$  is positive for all simulations, indicating that the brush grows throughout the evolution of the turbulent flame and the behaviour and contribution of each term is similar across simulations, once normalized by the initial turbulence intensity. As time progresses,  $d\delta/dt$  approaches zero, indicating that the brush thickness reaches a limit value, consistent with the temporal evolution of  $\delta$  in figure 8(b).

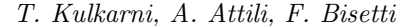
Early in the evolution, turbulent transport (term I) dominates and contributes to the growth of the flame brush. The contribution of term I decreases in magnitude as time progresses due to the decay of turbulence and associated decrease in the fluctuation u'. Throughout the simulations, differential stretch (term IV) is negative, slowing down the rate of growth of the brush. Its magnitude grows in absolute value as time progresses. The sum of terms II (mean velocity) and III (flame propagation) is positive, but of limited importance until much later in all simulations, when u' is small.

This analysis demonstrates that the growth rate of the flame brush thickness in this configuration is controlled by the balance between two mechanisms: turbulent transport contributing to the growth of the brush and differential flame stretch impeding the growth. The turbulent flame brush approaches a constant thickness when the two contributions become equal in magnitude, but opposite in sign. These two primary mechanisms are discussed separately next.

#### 6.1.2. Turbulent transport (term I)

The turbulent transport term is purely hydrodynamic and largely consistent with the theory of turbulent diffusion in isothermal flows. Multiplying and dividing term I by u'(t) and changing the variable of integration from r to  $\vartheta$ , we obtain

term I = 
$$(2\pi/\delta) \int_0^\infty \langle u_r' \rangle_w (r - R) \mathcal{P}_\phi dr$$
  
=  $\sqrt{2\pi} u' \int_{-u/\sigma}^\infty \frac{\langle u_r' \rangle_w}{u'} \vartheta \{\sigma \mathcal{P}_\theta(\vartheta)\} d\vartheta$ . (6.7)



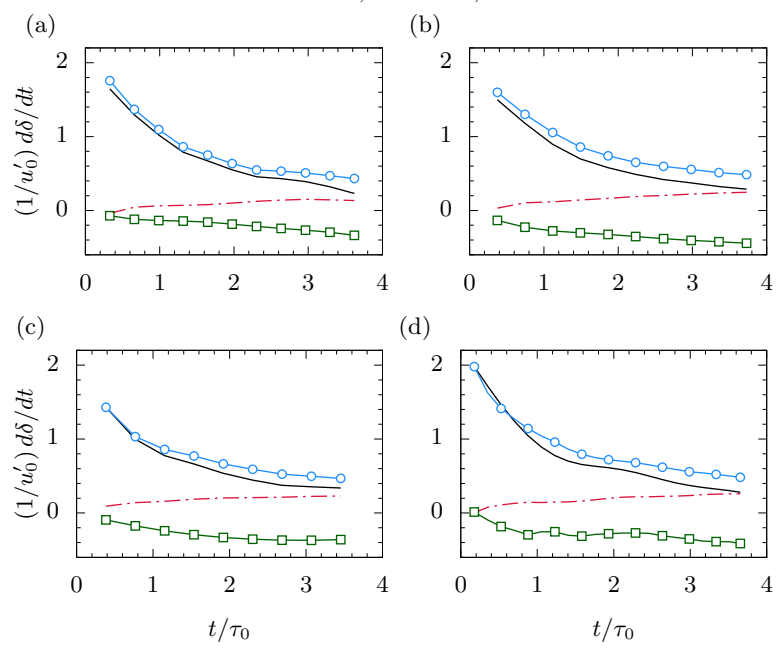


FIGURE 12. Contributions of different mechanisms in (6.6) to the growth of the flame brush thickness:  $d\delta/dt$  —, turbulent transport (term I) — , mean convection and mean propagation (sum of terms II and III) — · —, and differential stretch (term IV) — — . All terms are normalized by the initial turbulence intensity  $u_0'$ . Data shown for (a) R1, (b) R2, (c) R3, and (d) R2a.

Samples of the normalized surface averaged radial velocity fluctuation  $\langle u'_r \rangle_w / u'$  versus the normalized distance  $\vartheta$  are shown in figure 13(a), demonstrating a convincing collapse in time and across simulations. Especially in the middle of the brush for  $|\vartheta| \leq 2$ ,  $\langle u'_r \rangle_w / u'$  is a function of  $\vartheta$  only. Further, since  $\sigma \mathcal{P}_{\theta}$  is well approximated by the standard normal distribution (see §5.3) and constant in time, the integral in (6.7) is constant and term I is proportional to u' and depends on time only due to the fact that u' = u'(t) in decaying turbulence.

The fact that term I brings  $d\delta/dt \sim u'(t)$  is consistent with turbulent diffusion theory and (6.1). Indeed, figure 13(b) demonstrates a very close agreement between term I and (6.1) where the integral is evaluated with a model for Lagrangian autocorrelation coefficient in decaying turbulence (Huang & Leonard 1995). Further, the agreement in figure 13(b) points to the fact that the orientation factor  $\langle \cos \alpha_{p,t} \rangle$  in (6.3) is sufficiently close to unity for all practical purposes.

### 6.1.3. Differential flame stretch (term IV)

The differential flame stretch term reads

term IV = 
$$\delta \int_{-\mu/\sigma}^{\infty} \langle K' \rangle_w \vartheta^2 \sigma \mathcal{P}_{\theta} \, d\vartheta$$
 (6.8)  
=  $\delta \int_{-\mu/\sigma}^{\infty} (\langle a \rangle_w - K_G^a) \vartheta^2 \sigma \mathcal{P}_{\theta} \, d\vartheta + \delta \int_{-\mu/\sigma}^{\infty} (\langle -2S\kappa \rangle_w - K_G^{\kappa}) \vartheta^2 \sigma \mathcal{P}_{\theta} \, d\vartheta$ , (6.9)

## Reynolds scaling of turbulent burning rates

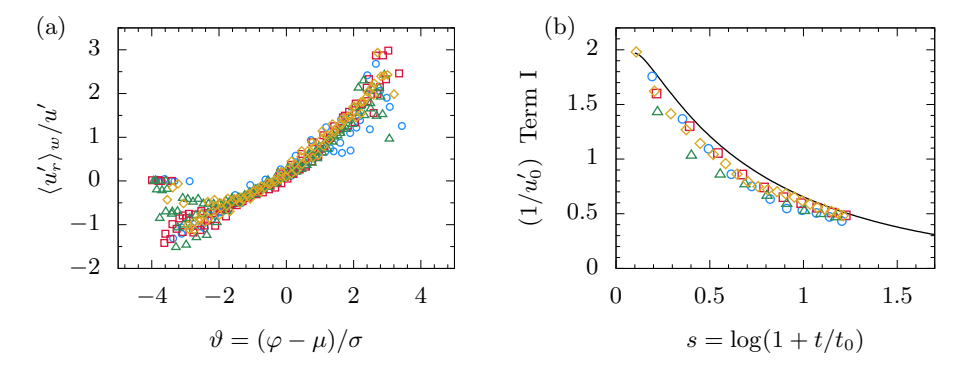


FIGURE 13. (a) Surface average of the radial velocity fluctuation scaled by the instantaneous fluctuation u'(t). (b) Comparison of (6.7) (symbols) with the prediction from (6.4) (solid line): R1  $(\bigcirc)$ , R2  $(\bigcirc)$ , R2a  $(\diamondsuit)$ , and R3  $(\triangle)$ .

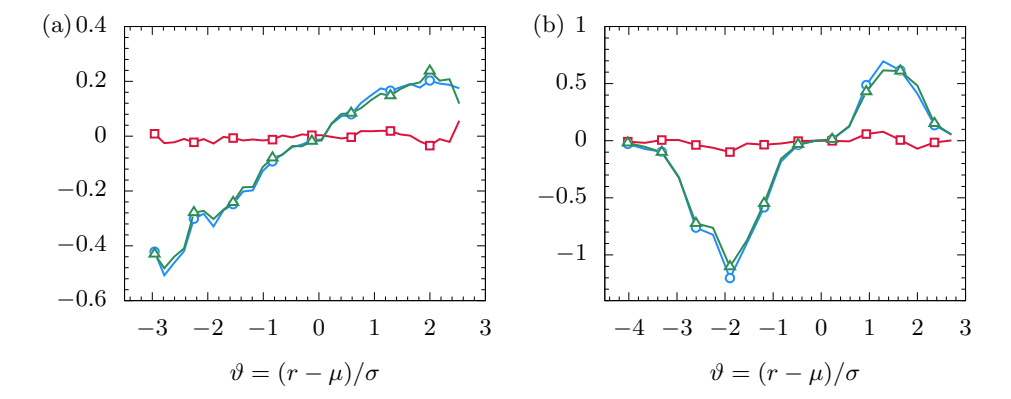


FIGURE 14. Analysis of the contributions to term IV for simulation R2 at a representative time. (a) Differential stretch  $\langle K \rangle_w - K_G (\bigcirc)$  and its components across the flame brush:  $\langle a \rangle_w - K_G^a (\square)$  and  $\langle -2S\kappa \rangle_w - K_G^\kappa (\triangle)$ . Normalization is by  $\tau_\eta^0$ . (b) The integrand in (6.8) ( $\bigcirc$ ) and the integrands in terms IVa ( $\square$ ) and IVb ( $\triangle$ ), all normalized by initial turbulence intensity  $u_0'$ .

where

$$K_G^a = (4\pi/A) \int_0^\infty r^2 \Sigma \langle a \rangle_w \, dr \tag{6.10}$$

$$K_G^{\kappa} = (4\pi/A) \int_0^\infty r^2 \Sigma \langle -2S\kappa \rangle_w \, dr \tag{6.11}$$

are the two components of the global stretch  $K_G = K_G^a + K_G^{\kappa}$  due to tangential strain and the propagative mechanism, respectively. The first and second terms on the r.h.s of (6.9) will be referred to as term IVa and term IVb, respectively.

Term IV depends on time because both  $\delta$  and  $\langle K' \rangle_w$  depend on time, while  $\sigma \mathcal{P}_{\theta}$  is well approximated by the standard normal distribution and constant. From the definition of  $\langle K' \rangle_w = \langle K - K_G \rangle_w = \langle K \rangle_w - K_G$ , it is apparent that if the statistics of flame stretch were spatially homogeneous, i.e.  $\langle K \rangle_w = K_G$ , surface stretch would not contribute to variations in the turbulent brush thickness. Instead, figure 14(a) shows that  $\langle K' \rangle_w$  is negative for  $\vartheta < 0$  and positive for  $\vartheta > 0$ , changing its sign at a location that is close to the flame's mean radius  $(\vartheta = 0)$ .

Furthermore, it is only the contribution of the propagative term  $-\langle 2S\kappa \rangle_w$  to differential

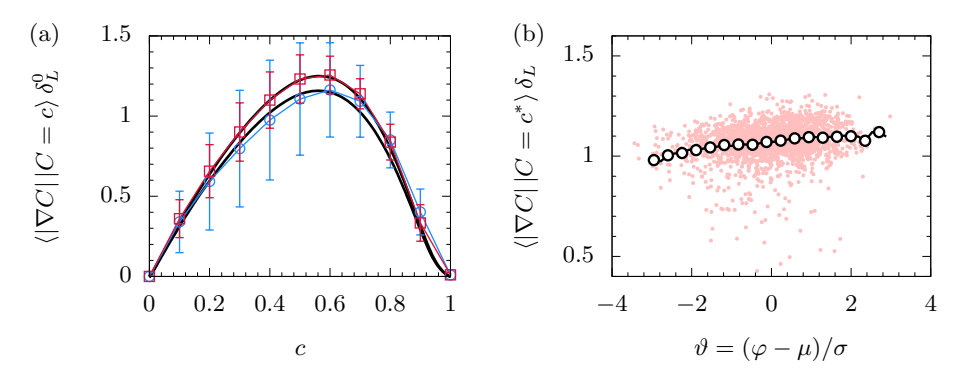


FIGURE 15. Conditional statistics of the gradient magnitude. Data from simulation R2. (a) Conditional mean gradient magnitude from DNS (blue and red lines), one-dimensional laminar flame (black lines) at two different times, normalized by the thermal thickness of the laminar flame  $\delta_L^0$ . Data shown at  $t/\tau_0=0.75$  (blue line with open circles) and  $t/\tau_0=5.25$  (red line with open squares). The error bars represent the conditional standard deviation. (b) Radial distribution of the conditional mean gradient magnitude ( $C=c^*$ ) at  $t/\tau_0=5.25$ . Scatter of samples is represented with small solid circles. Gradients are multiplied by the laminar flame thermal thickness  $\delta_L(t)$ .

stretch that is non-zero and governs the sign of  $\langle K' \rangle_w$ . This is due to the fact that the tangential rate of strain  $\langle a \rangle_w$  is spatially homogeneous, so that the difference between its local and global (or volume-averaged) value is zero. Conversely,  $-\langle 2S\kappa \rangle_w$  is negative at the trailing edge of the brush and positive at the leading edge, as well documented in spherical (Shy *et al.* 1999, 2000) and planar (Trouvé & Poinsot 1994; Chakraborty & Cant 2005) flames.

As a result of the spatial distribution of  $\langle K' \rangle_w$ , the integrand on the r.h.s. of (6.8) is mostly negative inside the flame brush as shown in figure 14(b), resulting in term IV being negative (see figure 12). The negative contribution of term IV to  $d\delta/dt$  indicates that differential flame stretch  $\langle K' \rangle_w$  induces a reduction in the thickness of the turbulent flame brush.

## 6.2. Scaling of peak value of the surface density function

Next, we address the variation of the peak value of the surface density function across simulations with varying Reynolds number. The surface density function associated with the iso-surface C=c (Vervisch *et al.* 1995) reads:

$$\Sigma(r,t;c) = \langle |\nabla C||C = c \rangle \mathcal{P}_C(c;r,t), \qquad (6.12)$$

where  $\mathcal{P}_C$  is the probability density function (PDF) of the progress variable C and angular brackets denote ensemble averaging.

Figure 15(a) shows  $\langle |\nabla C|| C=c \rangle$  as a function of c at early times  $(t/\tau_0=0.75)$  and towards the end  $(t/\tau_0=5.25)$  of simulation R2. The conditional mean of the gradient is very close to that found across the one-dimensional laminar flame, confirming that the turbulent flames belong to the thin flamelet regime (Peters 2000). Furthermore, at each instant, the gradient is normalized by  $\delta_L^0$  in order to highlight that the effect of pressure on the flame structure is minor as the peak value of the gradient changes by 10% only. Figure 15(b) shows the radial variation of  $\langle |\nabla C|| C=c^* \rangle$  across the brush at  $t/\tau_0=5.25$ , indicating that the conditional gradient magnitude grows only very slightly across the brush and may be considered constant for all practical purposes.

Thus, we conclude that the conditional gradient magnitude  $\langle |\nabla C||C=c^*\rangle$  is indepen-

#### Reynolds scaling of turbulent burning rates

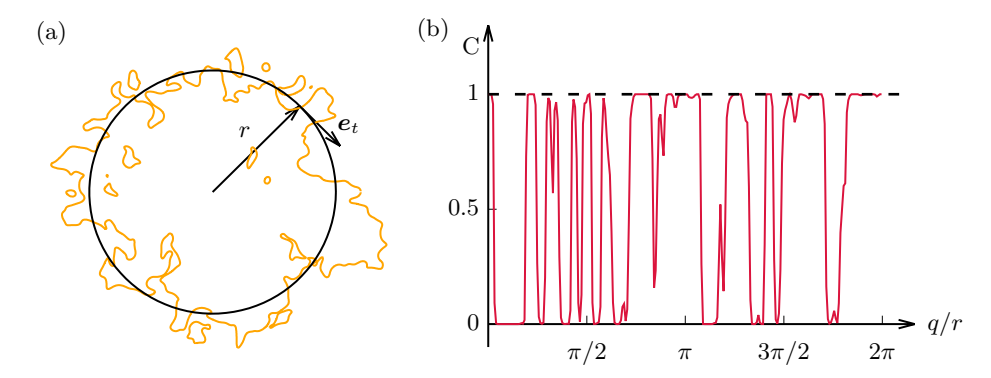


FIGURE 16. Flame surface crossings in a plane for simulation R2 at  $t/\tau_0 = 4.5$ . (a) Cut of the flame surface  $C = c^*$ . (b) Progress variable field along a circle of radius r versus the normalized arc length q/r.

dent of radial location r and time t also, so that any spatial and temporal dependence of the surface density function  $\Sigma$  is due to  $\mathcal{P}_{C}(c^{*}; r, t)$ .

In order to investigate the scaling and spatial dependence of  $\mathcal{P}_C$ , we consider an ensemble of two-dimensional plane cuts, whereby each plane contains the origin and its normal is oriented randomly. On each plane cut, we consider a circle of radius r, centred at the origin, and let  $e_t$  be the unit vector along the tangential direction. Let q be the arc length distance from an arbitrary point along the circle  $(0 \le q < 2\pi r)$ . Figure 16(a) shows a schematic representation of one such planar cut. The progress variable C as a function of the coordinate q along one such circles is shown in figure 16(b).

Given the spherical symmetry of the statistics, the progress variable C and its gradient  $\nabla C$  are ergodic along  $e_t$ . The probability  $\mathbb{P}$  that C takes a value between c - dc/2 and c + dc/2 on the circle is

$$\mathbb{P}[c - dc/2 \leqslant C \leqslant c + dc/2] = \mathcal{P}_C(c; r, t)dc = \frac{1}{p2\pi r} \sum_{i=1}^p \sum_{j=1}^{m_j} dq_{ij}, \tag{6.13}$$

where  $dq_{ij}$  is an infinitesimal arc length centred at location  $q_{ij}$  such that  $C(q_{ij}) = c$  and  $c - dc/2 \le C(q) \le c + dc/2$  for  $q_{ij} - dq_{ij}/2 \le q \le q_{ij} + dq_{ij}/2$  and  $m_j$  is the number of locations along circle j (j = 1, ..., p). Similar to the nomenclature used in the Bray-Moss-Libby (BML) model (Bray & Moss 1977; Libby & Bray 1980), each of the  $q_{ij}$  locations is referred to as a flame crossing.

Each infinitesimal arc length  $dq_{ij}$  is related to the projection of the gradient  $\nabla C$  onto the tangential vector  $\mathbf{e}_t$  at the flame crossing i with circle of radius r on plane j:

$$dq_{ij} = dc/|\nabla C \cdot \mathbf{e}_t|_{ij}. \tag{6.14}$$

Letting m indicate the total number of flame crossings summed over all planes

$$m = \sum_{j=1}^{p} m_j, (6.15)$$

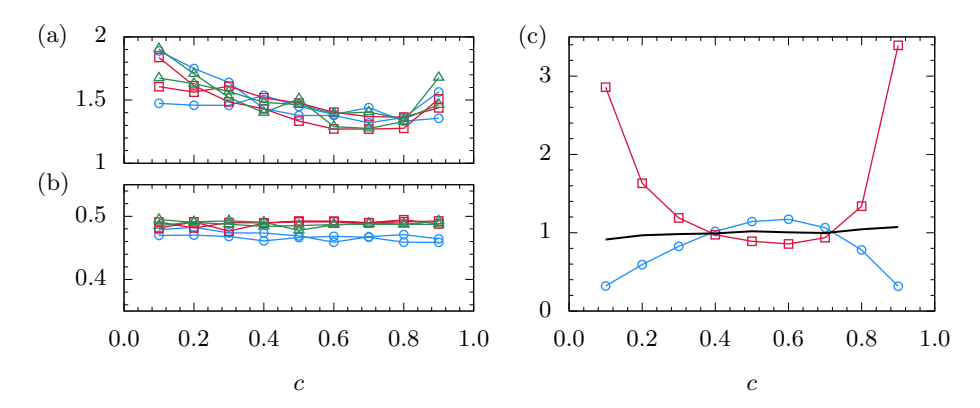


FIGURE 17. (a) Correction factor  $\Upsilon$  and (b) alignment  $\langle |\cos \alpha_{nt}||C=c \rangle$  statistics for three simulations at two select times: R1 ( $\bigcirc$ ), R2 ( $\square$ ), and R3 ( $\triangle$ ). (c) Peak surface density function  $\Sigma_m$  (thick line), PDF of progress variable  $\mathcal{P}_C$  ( $\square$ ), and conditional mean of the gradient magnitude  $\langle |\nabla C||C=c \rangle$  ( $\bigcirc$ ) at r=R(t), normalized by their corresponding values for  $c=c^*$ . Data from simulation R2.

rearranging (6.13), and dividing by dc, we have

$$\mathcal{P}_C(c; r, t) = \frac{m}{p2\pi r} \frac{1}{m} \sum_{i=1}^p \sum_{i=1}^{m_j} |\nabla C \cdot \mathbf{e}_t|_{ij}^{-1}$$
(6.16)

$$= \varpi(r,t) \langle |\nabla C \cdot \mathbf{e}_t|^{-1} | C = c \rangle, \tag{6.17}$$

where  $\varpi(r,t) = m/(p2\pi r)$  is the flame crossing frequency, defined as the number of flame crossings per unit length. The average of  $|\nabla C \cdot \mathbf{e}_t|^{-1}$  over all crossings on circles of radius r is simply the conditional average of  $|\nabla C \cdot \mathbf{e}_t|^{-1}$  at the radial location r.

Since the expression for  $\Sigma$  involves the conditional mean of  $|\nabla C|$ , it is beneficial to relate the conditional mean of the inverse  $|\nabla C \cdot e_t|^{-1}$  to the inverse of the conditional mean directly as

$$\langle |\nabla C \cdot \mathbf{e}_t|^{-1} | C = c \rangle = \Upsilon \langle |\nabla C \cdot \mathbf{e}_t| | C = c \rangle^{-1}, \tag{6.18}$$

where  $\Upsilon$  is a correction factor

$$\Upsilon = 1 + \operatorname{Var} \{ |\nabla C \cdot \mathbf{e}_t| |C = c \} / \langle |\nabla C \cdot \mathbf{e}_t| |C = c \rangle^2 + \dots$$
 (6.19)

We find that  $\Upsilon \approx 1.35$  for  $0.5 \leqslant c \leqslant 0.9$  across all simulations at all times as shown in figure 17(a). In the limit of infinitesimally thin turbulent premixed flames,  $\Upsilon \to 1$ .

Assuming that the projection of the flame normal n onto  $e_t$  and the gradient magnitude are uncorrelated, we write

$$\langle |\nabla C| | \boldsymbol{n} \cdot \boldsymbol{e}_t | |C = c \rangle \approx \langle |\nabla C| |C = c \rangle \langle |\boldsymbol{n} \cdot \boldsymbol{e}_t | |C = c \rangle.$$
 (6.20)

The assumption that the two are uncorrelated appears to be reasonable on the account that turbulence in the reactants is isotropic. Then,  $\mathcal{P}_C$  reads

$$\mathcal{P}_C(c; r, t) = \frac{\varpi(r, t)\Upsilon}{\langle |\nabla C||C = c\rangle \langle |\cos \alpha_{nt}||C = c\rangle},$$
(6.21)

where  $|\boldsymbol{n} \cdot \boldsymbol{e}_t| = |\cos \alpha_{nt}|$  and  $\alpha_{nt}$  is the angle between the normal  $\boldsymbol{n}$  and the ergodic direction  $\boldsymbol{e}_t$  and represents the orientation of the flamelets with respect to the ergodic direction. We find that the orientation angle  $\alpha_{nt}$  is nearly constant in time, independent of the conditioning value c, and the same across simulations. As a result,  $\Sigma$  is independent

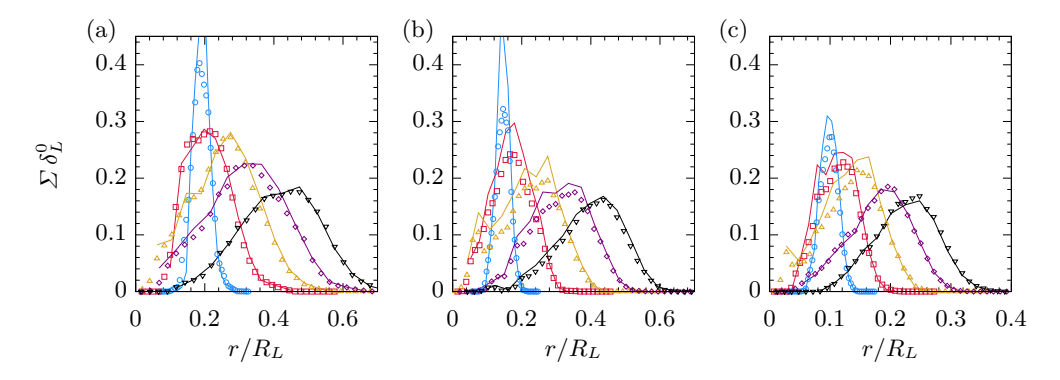


FIGURE 18. Comparison between the two expressions for  $\Sigma$  in (6.22) and (5.1) for three simulations at five times: (a) R1 (b) R2 and (c) R3. Time increases from left to right.

of the conditioning value c for  $0.1 \le c \le 0.9$  as shown in figure 17(c), since  $\mathcal{P}_C \sim 1/\langle |\nabla C|| C = c \rangle$ .

Based on the above analysis, an approximate expression for the surface density function is

$$\Sigma(r,t;c) = \varpi(r,t)\Upsilon/\langle|\cos\alpha_{nt}||C=c\rangle. \tag{6.22}$$

Figure 18 compares the left and right hand sides of (6.22) for c = 0.73, which are found to be in good agreement. Since the factor  $\Upsilon/\langle |\cos \alpha_{nt}|| C = c \rangle$  is approximately constant in space, time, and across simulations, the spatial and temporal dependence of  $\Sigma = \Sigma(r,t)$  is solely due to that of the crossing frequency  $\varpi = \varpi(r,t)$ .

This result is consistent with the Bray-Moss-Libby theory of turbulent premixed combustion, whereby the surface density function is modeled in terms of the spatial crossing frequency and a mean cosine factor as  $\Sigma = \varpi/\langle |cos\alpha_{nt}| \rangle$  (Bray et al. 1984; Bray & Libby 1986). Here we find a similar expression with the additional factor  $\Upsilon = \mathcal{O}(1)$ , which provides a correction for the fact that premixed flames are not infinitesimally thin and  $\Upsilon$  is not strictly unity.

For a statistically stationary and planar turbulent premixed flame, the BML model relates the crossing frequency  $\varpi$  to the two-point, one-time autocorrelation function of the progress variable

$$\mathcal{F}(q; x_1) = \langle C'(\boldsymbol{x}, t)C'(\boldsymbol{x} + q\boldsymbol{e}_{\alpha}, t) \rangle / \sigma_C^2$$
(6.23)

$$\varpi = \varpi(x_1) = -2 \left. \frac{\partial \mathcal{F}}{\partial q} \right|_{q=0},$$
(6.24)

where  $x_1$  is the inhomogeneous coordinate normal to the plane of the flame,  $C' = C - \langle C \rangle$  is the fluctuation field,  $\sigma_C^2 = \langle (C - \langle C \rangle)^2 \rangle$  is the variance, and  $e_\alpha$  is a unit vector in the plane of the flame that identifies an ergodic direction. Under specific assumptions on the functional form of the autocorrelation function  $\mathcal{F}$ , the crossing frequency and surface density function read

$$\overline{\omega} = A_{\overline{\omega}} \langle C \rangle (1 - \langle C \rangle) / L^*,$$
(6.25)

$$\Sigma = A_{\Sigma} \langle C \rangle (1 - \langle C \rangle) / L^*, \tag{6.26}$$

where  $\langle C \rangle = \langle C \rangle(x_1)$ ,  $A_{\varpi}$  and  $A_{\Sigma}$  are constants of order unity, and  $L^*$  is the so-called wrinkling scale.

Since the crossing frequency is closely related to the autocorrelation function of the progress variable (Bray et al. 1984; Bray & Libby 1986),  $L^*$  likely reflects the entire spectrum of the progress variable turbulent field C(x, t), although it is not clear how  $L^*$ 

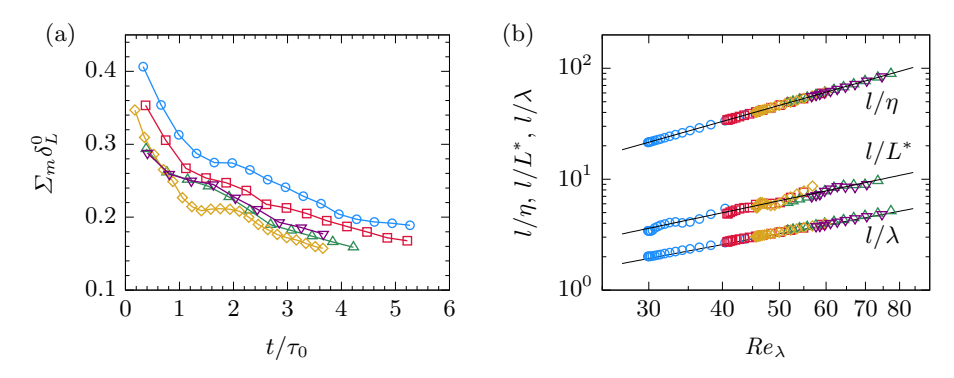


FIGURE 19. (a) Peak flame surface density  $\Sigma_m$  normalized by the thermal flame thickness  $\delta_L^0$ . (b) Ratio of length scales and power law fits  $aRe_{\lambda}^b$  (solid lines). We observe  $l/\eta \sim Re_{\lambda}^{1.5}$ ,  $l/\lambda \sim Re_{\lambda}^{1.0}$ , and  $l/L^* \sim Re_{\lambda}^{1.13}$ . Thus,  $L^*$  lies between  $\eta$  and  $\lambda$  with separation increasing with  $Re_{\lambda}$ . Symbols in both (a) and (b) represent data from various simulations: R1 ( $\bigcirc$ ), R2 ( $\square$ ), R2a ( $\diamondsuit$ ), R3 ( $\triangle$ ), and R3s ( $\bigcirc$ ).

should scale with the Reynolds number and how a suitable autocorrelation length could be defined from the autocorrelation function.

There exists significant controversy on the origin and values taken by the wrinkling scale in the literature. Cant & Bray (1989) proposed the following closure for the wrinkling scale,

$$L^* \propto k^{3/2} \epsilon^{-1},\tag{6.27}$$

thereby advancing the hypothesis that the wrinkling scale is proportional to the integral scale defined as  $l=u'^3/\epsilon$  and controlled by turbulence and energy-containing fluid motions, rather than flame propagation. Deschamps et al. (1992) observed  $L^*\approx l$  for conical turbulent premixed flames, while others (Veynante et al. 1994; Shy et al. 2000) found that the wrinkling scale is about five times smaller than the integral scale for V-shaped and planar turbulent premixed flames. Further, Shy et al. (2000) reported that the wrinkling scale remained constant for two different turbulence intensities, while the integral length scale changed by  $\approx 50\%$ . However, inadequate resolution of the turbulent flame surface may be responsible for this observation, as the wrinkling scale was found to be of the size as the width of the averaging box used for the measurement of the surface density function. Finally, dependence of  $L^*$  on  $u'/S_L$  has been postulated also, yet no conclusive evidence exists.

Given that  $L^*$  and  $1/\Sigma$  are related to within constants of order unity, we define the wrinkling scale as  $L^* = (4\Sigma_m)^{-1}$ , where  $\Sigma_m$  is the peak surface density in (5.20). The factor of 4 is included so as to be consistent with (6.26), since the peak surface density  $\Sigma_m$  occurs near  $\langle C \rangle = 0.5$ . The proportionality  $L^* \propto 1/\Sigma_m$  highlights that both quantities obey the same scaling laws.

Figure 19(a) shows the temporal evolution of  $\Sigma_m$  normalized by the thermal thickness of the laminar premixed flame. It is apparent that  $\Sigma_m$  decreases in time several-fold for each simulation. Because  $\delta_L^0$  is constant across simulations and the variation in the flame thickness is minimal during the propagation of the turbulent flames, figure 19(a) shows conclusively that  $\Sigma_m$  does not scale with the thermal thickness of the laminar flame.

This behavior is consistent with experiments on turbulent spherical flames in decaying turbulence behind grids (Renou *et al.* 2002; Fries *et al.* 2019). However, other experimental studies on turbulent propane/air flames in fan stirred spherical vessels (Bradley

et al. 2009) found that the peak surface density increased with time for some cases (rich mixtures at atmospheric pressures), while it decreased for others (at elevated pressures).

Figure 19(b) shows  $L^*$  normalized by the integral scale l and plotted against  $Re_{\lambda}$ . Data from all flame configurations and several times during each simulation are shown. It is apparent that over the range  $30 \leq Re_{\lambda} \leq 85$ ,  $L^*$  is about 5 to 10 times smaller than the integral length scale. Further, the wrinkling scale falls between the Taylor scale  $\lambda$  and Kolmogorov scale  $\eta$ , albeit closer to the former than to the latter. When scaled with l, the data suggest the following power law fit for the wrinkling scale

$$l/L^* = 4\Sigma_m l = 0.0756 Re_{\lambda}^{1.13}.$$
 (6.28)

Note that only data for  $t/\tau_0 > 0.5$  have been used in the fit since it is necessary for turbulent motions to wrinkle the flame past an initial transient, during which a power law scaling for  $l/L^*$  is not warranted.

The power law scaling from (6.28) shown in figure 19(b) is rather convincing, especially because it holds across simulations and *instantaneously* even as  $Re_{\lambda}$  and l vary in time during the decay of turbulence. Nonetheless, studies over a broader range of Reynolds number are obviously desirable.

The observation that  $\eta < L^* < \lambda$  suggests that the peak surface density is governed by small scales. The importance of small scales in controlling  $\Sigma_m$  has been postulated by Huh et al. (2013), who analysed the surface density transport equation for statistically planar flames and proposed that  $\Sigma_m$  scales with the inverse of the mean flame surface curvature. Since Zheng et al. (2017) demonstrated that the PDF of the flame surface curvature is independent of the Reynolds number when normalized with the Kolmogorov length, a case could be made that  $\Sigma_m \propto \eta^{-1}$ , independently of  $Re_{\lambda}$ . Our data do not support this conclusion, although they do highlight the fact that  $L^*$  is smaller than  $\lambda$  and its evolution is most likely related to processes at the dissipative end of the inertial range of the turbulence spectrum.

## 6.3. Scaling of the area ratio

The findings in  $\S 6.1$  and  $\S 6.2$  have critical implications with regard to the evolution of the area ratio  $\chi$  and its values across flame configurations. We begin by rearranging (5.21) into

$$\chi = \Sigma_m \delta \beta = (l/4L^*) (\delta/l) \beta. \tag{6.29}$$

Recalling that  $\beta$  is a shape factor that is nearly constant and substituting the scaling laws for the brush and peak surface density function, we obtain

$$\chi(t) = C_{\chi} Re_{\lambda}^{1.13} f(s), \tag{6.30}$$

where  $C_{\chi}$  is a constant and the dependence of  $\delta/l$  on time is captured by f(s) with  $s = \log(1 + t/t_0)$  indicating the transformed time coordinate.  $\chi$  and  $S_T/S_L \sim \chi$  depend on time directly due to  $\delta/l \sim f(s)$  and indirectly due to  $Re_{\lambda} = Re_{\lambda}(t)$  in decaying turbulence. The most important implication of (6.30) is that

$$\chi(t)Re_{\lambda}^{-1.13} \sim f(s) \tag{6.31}$$

only, so that if two turbulent spherical flames are compared at the same logarithmic time s, the area ratio  $\chi$  scales as  $Re_{\lambda}^{1.13}$  or as  $Re^{0.56}$ , since  $Re=u'l/\nu\sim Re_{\lambda}^2$ .

Figure 20(a) shows that  $\chi$  varies in time and across flame configurations. For  $t/\tau_0 > 2$ ,  $\chi$  reaches a limit value, which differ for each case by as much as a factor of 1.6. The same data are shown in compensated form as  $\chi(t)Re_{\lambda}^{-1.13}$  versus s in figure 20(b). Note that only data for  $t/\tau_0 > 0.5$ , which corresponds to s > 0.3, are shown because the scaling of

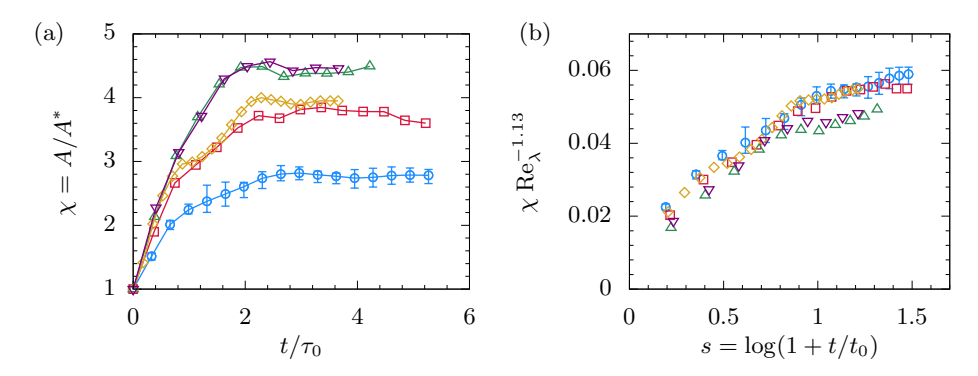


FIGURE 20. (a) Area ratio versus time  $t/\tau_0$ . (b) Area ratio compensated with the proposed Reynolds scaling versus the transformed time coordinate  $s = \log(1 + t/t_0)$  with  $t_0 = n\tau_0$ . Symbols represent data from simulations: R1 ( $\bigcirc$ ), R2 ( $\bigcirc$ ), R2a ( $\diamondsuit$ ), R3 ( $\triangle$ ), and R3s ( $\bigcirc$ ).

 $\Sigma_m$  implies that turbulent motions have had sufficient time to wrinkle the flame past an initial transient, during which the power law scaling  $l/L^*$  in (6.28) is not applicable.

The collapse in figure 20(b) is encouraging, albeit not perfect, especially for the data from simulations R3 and R3s at later times s > 1. Despite minor inconsistencies, which are related to the imperfect collapse of  $\delta/l$  at later times as shown in figure 11(b), we conclude that scale separation, as parametrized by the Reynolds number, is largely responsible for increasing the area ratio and the dimensionless turbulent flame speed  $S_T/S_L \sim \chi$  across flame configurations.

The fact that  $S_T/S_L \sim \chi \sim Re^{0.56}$  appears to contradict the notion that  $S_T/S_L$  depends on  $u'/S_L$  only. In order to investigate this important implication, three simulations are considered. These include R2 and R2a, which share the same Reynolds number, but not the same  $u'/S_L$ , and simulations R1 and R2a, which share  $u'/S_L$ , but not the same Reynolds number. Note that  $u'/S_L$  changes in time as reported in figure 4(c).

From the evolution of  $\chi$  for R1, R2, and R2a in figure 20(a), it is clear that when the Reynolds number is held constant and  $u'/S_L$  changes (R2 vs. R2a), the area ratio does not change. On the other hand, when  $u'/S_L$  is held constant and the Reynolds number changes (R1 vs. R2a), the area ratio is greater for the flame with the higher Reynolds number. These conclusions and observations support the hypothesis that  $S_T/S_L$  is not a function of  $u'/S_L$  independently of Reynolds number for the flame configuration considered.

The Reynolds dependence of turbulent burning rates has been observed for spherical flames elsewhere. Chaudhuri et al. (2011) proposed such scaling starting from the level set approach. Later, the same authors processed data from the experiments of Kobayashi et al. (1996, 2005) and showed convincing evidence that burning rates conform to the scaling  $Re^{0.55}$  (Chaudhuri et al. 2012). Similarly, Ahmed & Swaminathan (2013, 2014) reported that  $S_T/S_L \sim Re_T^{0.55}$  based on numerical simulations of methane/air and hydrogen/air flames. Since  $Re_\lambda \sim Re^{1/2}$ , our results are consistent with previous observations.

In closing, we remark that in most experiments on turbulent premixed flames, the integral scale of the flow remains approximately constant as u' is varied by increasing flow rates or fan speeds. This occurrence is due to the fact that the integral scales are set by the geometrical details of the burner, turbulence-generating grids, or fans, which are held fixed for practical reasons. The consequence is that both  $u'/S_L$  and Re vary together in most studies. Assuming that l remains approximately constant as u' increases

holding kinematic viscosity (i.e. pressure) and burner geometry unchanged, one obtains  $S_T/S_L \sim (u'/S_L)^{0.55}$  since  $S_T/S_L \sim Re^{0.55}$ .

## 7. Summary and conclusions

The propagation of spherical turbulent premixed methane/air flames in decaying turbulence was investigated at different conditions via Direct Numerical Simulations. Each DNS features detailed finite rate chemistry for methane oxidation and mixture-average transport. The simulations are repeated for several values of the Taylor-scale Reynolds number  $Re_{\lambda}$ , where all properties of isotropic turbulence are defined in the reactants. By design, the extent of the turbulent flame is large compared to the integral length scale of turbulence, guaranteeing that the flame surface is wrinkled by motions across the entire spectrum of turbulence and that statistics are duly converged. The flames belong to the thin reaction zone regime of turbulent premixed combustion and are characterized by low values of the Karlovitz number, so that the dimensionless turbulent flame speed is equal to the area ratio, defined as the ratio of the area of the flame surface to a reference area based on the mean progress variable. Thus, enhancements to the burning rate are brought by flame wrinkling, folding, and streching.

The data are analysed within the formalism of the surface density function and under the assumption of spherical symmetry of the statistics. The analysis shows that the dimensionless turbulent flame speed is equal to the product of the flame brush thickness, the peak value of the surface density function and a nondimensional shape factor of order unity. This decomposition lies at the basis of our postulate that the area ratio of turbulent premixed flames increases for increasing scale separation.

Once scaled by the instantaneous value of the integral length scale and plotted versus a stretched logarithmic time coordinate consistent with the evolution of turbulent kinetic energy in decaying homogeneous isotropic turbulence, the flame brush thickness is found to be nearly self-similar across simulations, irrespective of the Reynolds number of the flow. This result is significant because it indicates that the extent of the turbulent flame brush is governed by the largest scales of the flow as suggested by past experiments.

An ordinary differential equation that describes the evolution of the brush thickness is derived and indicates that the growth of the brush is controlled primarily by the balance of two mechanisms. Turbulent diffusion by velocity fluctuations leads to an increase in the brush thickness, consistent with Taylor's theory of turbulent diffusion, while spatial variations of the statistics of flame stretch across the brush lead to a decrease in its thickness. Early in the evolution, the brush grows rapidly due to turbulent transport, but later the two contributions balance each other and the brush thickness appears to reach an asymptotic limit.

The surface density function reaches a maximum in the center of the turbulent flame brush and its peak value is found to decrease in time as the flame propagates outwards. Following the framework of the Bray-Moss-Libby model of turbulent premixed combustion, we relate the peak value of the surface density function to the flamelet spatial crossing frequency, so that its inverse is the wrinking length scale. The concept of wrinkling length is noteworthy because it allows to scale the surface density function across simulations.

For all cases, we find that the wrinking length is larger than the Kolmogorov scale, but smaller than the Taylor micro-scale, being closer to the latter than to the former. Most important, the ratio between the wrinking scale and the integral scale of the flow is proportional to  $Re_{\lambda}^{-1.13}$  across all simulations. This result identifies the wrinkling scale as a hydrodynamic scale related to turbulence and its spectrum.

The evolution and scaling of the brush and peak surface density function result in the dimensionless turbulent flame speed scaling as  $S_T/S_LRe_{\lambda}^{-1.13} \sim f(s)$ , where s is the suitable logarithmic time coordinate for decaying turbulence and f(s) is a function that describes the growth of the brush normalized by the integral scale. The scaling is shown to hold to a very good approximation over several cases with  $30 \le Re_{\lambda} \le 80$ .

At present, the origin of the value of the scaling exponent is unclear and it is possible that it is somewhat specific to the spherical flame configuration. Futhermore, the results shown pertain to a modest range of Reynolds numbers and little separation exists between the dissipative scales and the wrinkling scale. More definitive conclusions require higher values of the Reynolds number. Finally, the flame configurations feature low values of the Karlovitz number, so that it is unclear whether the ratio of the Kolmogorov time to the flame time scale plays an additional role in the scaling.

Despite the limitations in scope, our data indicate that scale separation, as parametrized by the Reynolds number, is resposible for controlling the burning rates of the spherical turbulent premixed flames at the conditions explored in the simulations. Broadly, the fact that  $S_T/S_L \sim Re_\lambda^{1.13}$  points to the key role of the integral length scale l and kinematic viscosity  $\nu$ , in addition to that of the velocity fluctuation u', which is well recognized in the literature. Our analysis provides a novel perspective that is consistent quantitatively with recent experimental results.

This material is based upon work supported in part by the National Science Foundation (NSF) under Grant No. 1805921. Numerical simulations were carried out on the "Shaheen" supercomputer at King Abdullah University of Science and Technology (KAUST) and on the "Stampede 2" supercomputer at the Texas Advanced Computing Center (TACC) through allocation TG-CTS18002 under the Extreme Science and Engineering Discovery Environment (XSEDE). XSEDE is supported by the NSF under Grant No. ACI-1548562. Any opinions, findings, and conclusions or recommendations expressed in this material are those of the author(s) and do not necessarily reflect the views of the NSF.

## Appendix A. Dispersion relation in spherical coordinate system

Taylor's theory of turbulent diffusion (Taylor 1922) describes the dispersion of material points in homogeneous isotropic turbulence. Its application to dispersion in radial coordinates requires modifications to account for changes in the radial direction along Lagrangian trajectories. Consider an ensemble of particles released on a sphere of radius  $R_0$  at time t=0 in decaying homogeneous isotropic turbulence. The radial distance r(a,t) of particle with index a at t>0 is given by

$$r(a,t) = |\boldsymbol{x}(a,t)|,\tag{A 1}$$

where x is the position vector of the particle with respect to the origin.

The evolution of the particle's radial distance is governed by

$$\frac{dr(a,t)}{dt} = \boldsymbol{u}(\boldsymbol{x}(a,t),t) \cdot \boldsymbol{i}_r(a,t), \tag{A 2}$$

where u denotes the local fluid velocity vector at the particle location and  $i_r$  is the unit vector in radial direction

$$\mathbf{i}_r(a,t) = \frac{\mathbf{x}(a,t)}{|\mathbf{x}(a,t)|}.$$
 (A3)

Integrating the ordinary differential equation with initial condition  $r(a,0) = R_0$  gives

39

the particle's distance for t > 0

$$r(a,t) = R_0 + \int_0^t \mathbf{u}(\mathbf{x}(a,p), p) \cdot \mathbf{i}_r(a,p) \, dp. \tag{A4}$$

Here p represents the dummy variable of integration.

Following Taylor (1922), the variance  $\sigma^2$  of the radial distance in the absence of mean radial velocity is

$$\frac{1}{2}\frac{d\sigma^2}{dt} = \left\langle (r(a,t) - R_0)\frac{dr}{dt}(a,t) \right\rangle = \left\langle \boldsymbol{u}(a,t) \cdot \boldsymbol{i}_r(a,t) \int_0^t \boldsymbol{u}(a,p) \cdot \boldsymbol{i}_r(a,p) \, dp \right\rangle, \quad (A.5)$$

since the mean radial distance is constant and equal to  $R_0$ . In the above expression, angular brackets denote average over the ensemble of particles and the dependence of  $\boldsymbol{u}$  on  $\boldsymbol{x}(a,p)$  is written as  $\boldsymbol{u}(a,p)$ .

The above integral reads:

$$\frac{1}{2} \frac{d\sigma^2}{dt} = \int_0^t \left\langle u_x(a,t) u_x(a,p) \frac{x(a,t)x(a,p)}{r(a,t)r(a,p)} \right\rangle dp$$

$$+ \int_0^t \left\langle u_y(a,t) u_y(a,p) \frac{y(a,t)y(a,p)}{r(a,t)r(a,p)} \right\rangle dp$$

$$+ \int_0^t \left\langle u_z(a,t) u_z(a,p) \frac{z(a,t)z(a,p)}{r(a,t)r(a,p)} \right\rangle dp,$$
(A 6)

where  $u_x, u_y, u_z$  and x, y, z denote the Cartesian components of vectors  $\boldsymbol{u}$  and  $\boldsymbol{x}$ , respectively.

In homogeneous turbulence, the velocity vector u is uncorrelated with the position vector x. Also, due to isotropicity, the Lagrangian autocorrelation functions of all components of velocity is the same. In light of these simplifications, the above equation becomes

$$\frac{1}{2}\frac{d\sigma^2}{dt} = \int_0^t \left\langle u_x(a,t)u_x(a,p) \right\rangle \left\langle \frac{\boldsymbol{x}(a,t) \cdot \boldsymbol{x}(a,p)}{|\boldsymbol{x}(a,t)| |\boldsymbol{x}(a,p)|} \right\rangle dp,\tag{A 7}$$

with a dependence on the mean cosine of the angle between radial vectors on Lagrangian trajectories. Simplifying the above as in Taylor (1922), we obtain

$$\frac{1}{2}\frac{d\sigma^2}{dt} = u'(t)\int_0^t u'(p)f_L(p,t)\langle\cos\alpha_{p,t}\rangle\,dp,\tag{A 8}$$

where  $f_L$  denotes the Lagrangian autocorrelation function in decaying isotropic turbulence

$$f_L(t_1, t_2) \equiv \frac{\left\langle u_x(a, t_1) u_x(a, t_2) \right\rangle}{u'(t_1) u'(t_2)},$$
 (A 9)

where u'(t) the turbulence intensity at time t.

In (A8),  $\alpha_{p,t}$  is the angle between position vectors on the Lagrangian trajectory at times t and p. This implies that Taylor's theory over-estimates the variance, since  $\cos \alpha_{p,t} \leq 1$ . The correction factor  $\langle \cos \alpha_{p,t} \rangle$  depends on the lateral movement of particles in the polar and azimuthal directions compared to that in the radial one and is close to unity for small values of the ratio between the two.

- ABDEL-GAYED, R. G. & BRADLEY, D. 1977 Dependence of turbulent burning velocity on turbulent reynolds number and ratio of flaminar burning velocity to r.m.s. turbulent velocity. Symp. (Int.) Combust. 16 (1), 1725 1735.
- ABDEL-GAYED, R. G., BRADLEY, D. & GRAY, P. 1981 A two-eddy theory of premixed turbulent flame propagation. *Phil. Trans. R. Soc. London, Ser. A* **301** (1457), 1–25.
- Ahmed, I. & Swaminathan, N. 2013 Simulation of spherically expanding turbulent premixed flames. *Combust. Sci. Technol.* **185** (10), 1509–1540.
- Ahmed, I. & Swaminathan, N. 2014 Simulation of turbulent explosion of hydrogen-air mixtures. *Int. J. Hydrog. Energy* **39** (17), 9562 9572.
- Albin, E. 2010 Contribution to numerical modelling of turbulent flames : DNS-EEM comparisons. PhD thesis, Rouen, INSA.
- Albin, E. & Dangelo, Y. 2012 Assessment of the evolution equation modelling approach for three-dimensional expanding wrinkled premixed flames. *Combust. Flame* **159** (5), 1932 1948.
- Andrews, G. E., Bradley, D. & Lwakabamba, S. B. 1975 Measurement of turbulent burning velocity for large turbulent reynolds numbers. Symp. (Int.) Combust. 15 (1), 655 664.
- ASHURST, W. T., KERSTEIN, A. R., KERR, R. M. & GIBSON, C. H. 1987 Alignment of vorticity and scalar gradient with strain rate in simulated Navier–Stokes turbulence. *Phys. Fluids* **30** (8), 2343–2353.
- ATTILI, A. & BISETTI, F. 2019 Statistics of scalar dissipation and strain/vorticity/scalar gradient alignment in turbulent nonpremixed jet flames. Flow Turbul. Combust. 103 (3), 625–642.
- BAINES, W. D. & PETERSON, E. G. 1951 An investigation of flow through screens. *Trans. Am. Soc. Mech. Engrs.* **73**.
- Barenblatt, G. I. 1996 Scaling, self-similarity, and intermediate asymptotics: dimensional analysis and intermediate asymptotics. Cambridge University Press.
- BATCHELOR, G. K. 1952 The effect of homogeneous turbulence on material lines and surfaces. *Proc. R. Soc. London, Ser. A* **213** (1114), 349–366.
- Batchelor, G. K. & Townsend, A. A. 1948a Decay of isotropic turbulence in the initial period. *Proc. R. Soc. London, Ser. A* 193 (1035), 539–558.
- BATCHELOR, G. K. & TOWNSEND, A. A. 1948b Decay of turbulence in the final period. *Proc. R. Soc. London, Ser. A* 194 (1039), 527–543.
- BATCHELOR, G. K. & TOWNSEND, A. A. 1956 Turbulent diffusion. In Surveys in Mechanics (ed. G. K. Batchelor & R. M. Davies). Cambridge University Press.
- BIRD, R. B., STEWART, W. E. & LIGHTFOOT, E. N. 2006 Transport phenomena, 2nd edn. Hoboken, New Jersey: John Wiley & Sons.
- Bradley, D., Lawes, M. & Mansour, M. S. 2009 Flame surface densities during spherical turbulent flame explosions. *Proc. Combust. Inst.* **32** (1), 1587–1593.
- Bray, K. N. C & Libby, P. A. 1986 Passage times and flamelet crossing frequencies in premixed turbulent combustion. *Combust. Sci. Technol.* 47 (5-6), 253–274.
- Bray, K. N. C., Libby, P. A. & Moss, J. B. 1984 Flamelet crossing frequencies and mean reaction rates in premixed turbulent combustion. *Combust. Sci. Technol.* **41** (3-4), 143–172.
- Bray, K. N. C. & Moss, J. B. 1977 A unified statistical model of the premixed turbulent flame. *Acta Astronaut.* 4 (3-4), 291–319.
- Buckingham, E. 1914 On physically similar systems; illustrations of the use of dimensional equations. *Phys. Rev.*  $\bf 4$ , 345.
- Candel, S. M. & Poinsot, T. 1990 Flame stretch and the balance equation for the flame area. Combust. Sci. Technol. 70, 1–15.
- Cant, R. S. & Bray, K. N. C. 1989 Strained laminar flamelet calculations of premixed turbulent combustion in a closed vessel. Symp. (Int.) Combust. 22 (1), 791–799.
- Chakraborty, N. & Cant, R. S. 2005 Effects of strain rate and curvature on surface density function transport in turbulent premixed flames in the thin reaction zones regime. *Phys. Fluids* 17 (6), 065108.
- Chatakonda, O., Hawkes, E. R., Aspden, A. J., Kerstein, A. R., Kolla, H. & Chen, J. H. 2013 On the fractal characteristics of low Damköhler number flames. *Combust. Flame* 160 (11), 2422–2433.

- Chaudhuri, S., Akkerman, V. & Law, C. K. 2011 Spectral formulation of turbulent flame speed with consideration of hydrodynamic instability. *Phys. Rev. E* 84 (2), 026322.
- Chaudhuri, S., Wu, F., Zhu, D. & Law, C. K. 2012 Flame speed and self-similar propagation of expanding turbulent premixed flames. *Phys. Rev. Lett.* **108** (4), 044503.
- CHORIN, A. J. 1968 Numerical solution of the Navier-Stokes equations. Math. Comput. 22, 745–762.
- CIFUENTES, L., DOPAZO, C., MARTIN, J. & JIMENEZ, C. 2014 Local flow topologies and scalar structures in a turbulent premixed flame. *Phys. Fluids* **26** (6), 065108.
- COCKE, W. J. 1969 Turbulent hydrodynamic line stretching: Consequences of isotropy. *Phys. Fluids* **12** (12), 2488–2492.
- Comte-Bellot, G. & Corrsin, S. 1971 Simple Eulerian time correlation of full-and narrow-band velocity signals in grid-generated, isotropic turbulence. J. Fluid Mech. 48 (2), 273–337.
- Damköhler, G. 1940 Der einflußder turbulenz auf die flammengeschwidigkeit in gasgemischen. Z. Elektrochem. 46, 601–652, 1947, English translation NASA Tech. Mem 1112.
- Deschamps, B., Boukhalfa, A., Chauveau, C., Gökalp, I., Shepherd, I. G. & Cheng, R. K. 1992 An experimental estimation of flame surface density and mean reaction rate in turbulent premixed flames. *Symp. (Int.) Combust.* **24** (1), 469–475.
- Desjardins, O., Blanquart, G., Balarac, G. & Pitsch, H. 2008 High order conservative finite difference scheme for variable density low Mach number turbulent flows. *J. Comput. Phys.* **227** (15), 7125–7159.
- DRISCOLL, J. F. 2008 Turbulent premixed combustion: Flamelet structure and its effect on turbulent burning velocities. *Prog. Energ. Combust. Sci.* **34** (1), 91–134.
- DRUMMOND, I. T. 1993 Stretching and bending of line elements in random flows. *J. Fluid Mech.* **252**, 479–498.
- DRUMMOND, I. T. & MÜNSCH, W. 1990 Turbulent stretching of line and surface elements. J. Fluid Mech. 215, 45–59.
- Fairweather, M., Ormsby, M. P., Sheppard, C. G. W. & Woolley, R. 2009 Turbulent burning rates of methane and methan–hydrogen mixtures. *Combust. Flame* **156** (4), 780–790.
- Falgout, R. D., Jones, J. E. & Yang, U. M. 2006 The design and implementation of Hypre, a library of parallel high performance preconditioners. In *Numerical solution of partial differential equations on parallel computers*, pp. 267–294. Springer.
- FRIES, D., OCHS, B., SAHA, A., RANJAN, D. & MENON, S. 2019 Flame speed characteristics of turbulent expanding flames in a rectangular channel. *Combust. Flame* **199**, 1–13.
- Frisch, U. 1995 Turbulence: the legacy of AN Kolmogorov. Cambridge University Press.
- GIRIMAJI, S. S. 1991 Asymptotic behavior of curvature of surface elements in isotropic turbulence. *Phys. Fluids* **3** (7), 1772–1777.
- GIRIMAJI, S. S. & POPE, S. B. 1990 Material-element deformation in isotropic turbulence. *J. Fluid Mech.* **220**, 427–458.
- GIRIMAJI, S. S. & POPE, S. B. 1992 Propagating surfaces in isotropic turbulence. *J. Fluid Mech.* **234**, 247–277.
- GOULDIN, F. C. 1987 An application of fractals to modeling premixed turbulent flames. Combust. Flame 68 (3), 249–266.
- HINDMARSH, A. C., BROWN, P. N., GRANT, K. E., LEE, S. L., SERBAN, R., SHUMAKER, D. E. & WOODWARD, C. S. 2005 SUNDIALS: suite of nonlinear and differential/algebraic equation solvers. *ACM Trans. Math. Software* **31**, 363–396.
- HINZE, J. O. 1975 Turbulence. New York: McGraw-Hill.
- HIRSCHFELDER, J., CURTISS, C., BIRD, R. & MAYER, M. 1954 Molecular theory of gases and liquids. Wiley New York.
- Huang, M. J. & Leonard, A. 1995 Velocity autocorrelations of decaying isotropic homogeneous turbulence. *Phys. Fluids* **7** (10), 2455–2464.
- Huh, K. Y., Kwon, J. & Lee, D. 2013 Relationships for maximum flame surface density and brush thickness through conditional analysis in turbulent premixed combustion. *Phys. Fluids* **25** (7), 075108.
- JOHNSON, N. L., KOTZ, S. & BALAKRISHNAN, N. 1994 Continuous univariate distributions, 2nd edn. Hoboken, NJ: Wiley-Interscience.

- Kim, J. & Moin, P. 1985 Application of a fractional-step method to incompressible navier-stokes equations. J. Comput. Phys. 59 (2), 308–323.
- KOBAYASHI, H., SEYAMA, K., HAGIWARA, H. & OGAMI, Y. 2005 Burning velocity correlation of methane/air turbulent premixed flames at high pressure and high temperature. *Proc. Combust. Inst.* **30** (1), 827–834.
- KOBAYASHI, H., TAMURA, T., MARUTA, K., NIIOKA, T. & WILLIAMS, F. A. 1996 Burning velocity of turbulent premixed flames in a high-pressure environment. *Symp. (Int.) Combust.* **26** (1), 389–396.
- LAWN, C. J. & SCHEFER, R. W. 2006 Scaling of premixed turbulent flames in the corrugated regime. *Combust. Flame* **146**, 180–199.
- LIBBY, P. A. & Bray, K. N. C. 1980 Implications of the laminar flamelet model in premixed turbulent combustion. *Combust. Flame* **39** (1), 33–41.
- Libby, P. A. & Williams, F. A. 1994 Turbulent reacting flows. Academic press.
- LIPATNIKOV, A. 2012 Fundamentals of premixed turbulent combustion. CRC Press.
- LIPATNIKOV, A. N. & CHOMIAK, J. 2002 Turbulent flame speed and thickness: phenomenology, evaluation, and application in multi-dimensional simulations. *Prog. Energ. Combust. Sci.* **28** (1), 1–74.
- LIPATNIKOV, A. N., LI, W. Y., JIANG, L. J. & SHY, S. S. 2017 Does density ratio significantly affect turbulent flame speed? Flow Turbul. Combust. 98, 1153–1172.
- Liu, C. C., Shy, S. S., Peng, M. W., Chiu, C. W. & Dong, Y. C. 2012 High-pressure burning velocities measurements for centrally-ignited premixed methane/air flames interacting with intense near-isotropic turbulence at constant Reynolds numbers. *Combust. Flame* 159, 2608–2619.
- LIU, X. D., OSHER, S. & CHAN, T. 1994 Weighted Essentially Non-oscillatory Schemes. J. Comput. Phys. 115, 200–212.
- Luca, S., Al-Khateeb, A. N., Attili, A. & Bisetti, F. 2018a Comprehensive validation of skeletal mechanism for turbulent premixed methaneair flame simulations. *J. Propul. Power* **34**, 153–160.
- Luca, S., Attili, A., Lo Schiavo, E., Creta, F. & Bisetti, F. 2018b On the statistics of flame stretch in turbulent premixed jet flames in the thin reaction zone regime at varying Reynolds number. *Proc. Combust. Inst.* 37 (2), 2451–2459.
- MACART, J. F. & MUELLER, M. E. 2016 Semi-implicit iterative methods for low Mach number turbulent reacting flows: Operator splitting versus approximate factorization. J. Comput. Phys. 326, 569–595.
- MANDELBROT, B. B. 1975 On the geometry of homogeneous turbulence, with stress on the fractal dimension of the iso-surfaces of scalars. *J. Fluid Mech.* **72** (3), 401–416.
- MARBLE, F. E. & BROADWELL, J. E. 1977 The coherent flame model for turbulent chemical reactions. *Tech. Rep.*. Purdue Univ Lafayette in Project Squid Headquarters.
- MATHUR, S., TONDON, P. K. & SAXENA, S. C. 1967 Thermal conductivity of binary, ternary and quaternary mixtures of rare gases. *Mol. Phys.* 12, 569–579.
- MAZ'JA, V. 1985 Sobolev spaces, chap. 1.2.4, p. 37. Springer.
- McBride, B. J., Gordon, S. & Reno, M. A. 1993 Coefficients for calculating thermodynamic and transport properties of individual species. *Tech. Rep.*. National Aeronautics and Space Administration, Technical Memorandum 4513.
- MOHAMED, M. S. & LARUE, J.C. 1990 The decay power law in grid-generated turbulence. *J. Fluid Mech.* **219**, 195–214.
- MUELLER, B. 1999 Low Mach number asymptotics of the Navier-Stokes equations and numerical implications. In *Lecture Series*, von Kármán Institute for Fluid Dynamics.
- NIVARTI, G. & CANT, S. 2017 Direct numerical simulation of the bending effect in turbulent premixed flames. *Proc. Combust. Inst.* **36** (2), 1903–1910.
- Peaceman, D. W. & Rachford, H. H. 1955 The numerical solution of parabolic and elliptic differential equations. J. Soc. Indust. Appl. Math. 3, 28–41.
- Peters, N. 1992 A spectral closure for premixed turbulent combustion in the flamelet regime. J. Fluid Mech. 242, 611–629.
- Peters, N. 2000 Turbulent Combustion. Cambridge University Press.
- Pierce, C. D. 2001 Progress-variable approach for large-eddy simulation of turbulent combustion. PhD thesis, Stanford University.

- POINSOT, T. & VEYNANTE, D. 2012 Theoretical and numerical combustion, 3rd edn. Toulouse, France: Centre Européen de Recherche et de Formation Avancée en Calcul Scientifique.
- POPE, S. B. 1988 The evolution of surfaces in turbulence. Int. J. Enq. Sci. 26 (5), 445–469.
- POPE, S. B. 2000 Turbulent flows. Cambridge, United Kingdom: Cambridge University Press.
- Renou, B., Mura, A., Samson, E. & Boukhalfa, A. 2002 Characterization of the local flame structure and the flame surface density for freely propagating premixed flames at various lewis numbers. *Combust. Sci. Technol.* **174** (4), 143–179.
- ROSALES, C. & MENEVEAU, C. 2005 Linear forcing in numerical simulations of isotropic turbulence: Physical space implementations and convergence properties. *Phys. Fluids* 17 (9), 095106.
- She, Z. S., Jackson, E., Orszag, S. A., Hunt, J. C. R., Phillips, O. M. & Williams, D. 1991 Structure and dynamics of homogeneous turbulence: models and simulations. *Proc. R. Soc. London, Ser. A* **434** (1890), 101–124.
- SHY, S.S., I, W. K., Lee, E. I. & Yang, T. S. 1999 Experimental analysis of flame surface density modeling for premixed turbulent combustion using aqueous autocatalytic reactions. *Combust. Flame* 118 (4), 606–618.
- SHY, S. S., LEE, E. I., CHANG, N. W. & YANG, S. I. 2000 Direct and indirect measurements of flame surface density, orientation, and curvature for premixed turbulent combustion modeling in a cruciform burner. *Proc. Combust. Inst.* 28 (1), 383–390.
- DE SILVA, C. M., PHILIP, J., CHAUHAN, K., MENEVEAU, C. & MARUSIC, I. 2013 Multiscale geometry and scaling of the turbulent-nonturbulent interface in high Reynolds number boundary layers. *Phys. Rev. Lett.* **111** (4), 044501.
- SINHUBER, M., BODENSCHATZ, E. & BEWLEY, G. P. 2015 Decay of turbulence at high Reynolds numbers. *Phys. Rev. Lett.* **114**, 034501.
- Sreenivasan, K. R. 1991 Fractals and multifractals in fluid turbulence. *Annu. Rev. Fluid Mech.* 23 (1), 539–604.
- SREENIVASAN, K. R. 1995 On the universality of the Kolmogorov constant. *Phys. Fluids* **7** (11), 2778–2784.
- Sreenivasan, K. R. & Meneveau, C. 1986 The fractal facets of turbulence. *J. Fluid Mech.* 173, 357–386.
- Tabor, M. & Klapper, I. 1994 Stretching and alignment in chaotic and turbulent flows. *Chaos Solitons Fract.* 4, 1031–1055.
- Taylor, G. I. 1922 Diffusion by continuous movements. *Proc. R. Soc. London, Ser. A* 2 (1), 196–212.
- Taylor, G. I. 1935 Statistical theory of turbulence. Proc. R. Soc. London, Ser. A 151 (873), 421–444.
- Tomboulides, A. G., Lee, J. C. Y. & Orszag, S. A. 1997 Numerical simulation of low Mach number reactive flows. *J. Sci. Comput.* 12 (2), 139–167.
- Trouvé, A. & Poinsot, T. 1994 The evolution equation for the flame surface density in turbulent premixed combustion. *J. Fluid Mech.* **278**, 1–31.
- TSINOBER, A. 2009 An Informal Conceptual Introduction to Turbulence. Netherlands: Springer. TSINOBER, A., KIT, E. & DRACOS, T. 1992 Experimental investigation of the field of velocity gradients in turbulent flows. J. Fluid Mech. 242, 169–192.
- VERVISCH, L., BIDAUX, E., BRAY, K. & KOLLMANN, W. 1995 Surface density function in premixed turbulent combustion modeling, similarities between probability density function and flame surface approaches. *Phys. Fluids* 7 (10), 24962503.
- Veynante, D., Duclos, J. M. & Piana, J. 1994 Experimental analysis of flamelet models for premixed turbulent combustion. Symp. (Int.) Combust. 25 (1), 1249–1256.
- VEYNANTE, D. & VERVISCH, L. 2002 Turbulent combustion modeling. *Prog. Energ. Combust. Sci.* **28**, 193–266.
- VINCENT, A. & MENEGUZZI, M. 1994 The dynamics of vorticity tubes in homogeneous turbulence. J. Fluid Mech. 258, 245–254.
- WILKE, C. R. 1950 A viscosity equation for gas mixtures. J. Chem. Phys. 18, 517–519.
- Williams, F. A. 1985 Turbulent combustion. In *The mathematics of combustion*, pp. 97–131. SIAM.
- WILLIAMS, F. A. 1994 Combustion Theory, 2nd edn. Westview Press.

Zheng, T., You, J. & Yang, Y. 2017 Principal curvatures and area ratio of propagating surfaces in isotropic turbulence. *Phys. Rev. Fluids* **2** (10), 103201.